

AD-A266 339



4

225300-8-F
Final Report

RADAR IMAGING OF SUB-MESOSCALE OCEAN PHENOMENA

D.R. Lyzenga

March 1993

DTIC
ELECTE
JUN 28 1993
S B D

Office of Naval Research
800 N. Quincy St.
Arlington, VA 22217-5660

Contract No. N00014-90-C-0071

DISTRIBUTION STATEMENT A
Approved for public release
Distribution Unlimited



P.O. Box 134001
Ann Arbor, MI 48113-4001

93-14583



93 6 325

REPORT DOCUMENTATION PAGE			Form Approved OMB No. 0704-0188	
<small>Public reporting burden for this collection of information is estimated to average 1 hour per response, including the time for reviewing instructions, searching existing data sources, gathering and maintaining the data needed, and completing and reviewing the collection of information. Send comments regarding this burden estimate or any other aspect of this collection of information, including suggestions for reducing this burden, to Washington Headquarters Services, Directorate for Information Operations and Reports, 215 Jefferson Davis Highway, Suite 1204, Arlington, VA 22202-4302, and to the Office of Management and Budget, Paperwork Reduction Project (0704-0188), Washington, DC 20503.</small>				
1. AGENCY USE ONLY (Leave blank)		2. REPORT DATE March 1993		3. REPORT TYPE AND DATES COVERED Final, Feb., 1990 - Jan., 1993
4. TITLE AND SUBTITLE Radar Imaging of Sub-Mesoscale Ocean Phenomena			5. FUNDING NUMBERS N00014-90-C-0071	
6. AUTHOR(S) Dave R. Lyzenga				
7. PERFORMING ORGANIZATION NAME(S) AND ADDRESS(ES) Environmental Research Institute of Michigan (ERIM) P.O. Box 134001 Ann Arbor, MI 48113-4001			8. PERFORMING ORGANIZATION REPORT NUMBER 225300-8-F	
9. SPONSORING / MONITORING AGENCY NAME(S) AND ADDRESS(ES) Office of Naval Research 800 N. Quincy St. Arlington, VA 22217-5660			10. SPONSORING / MONITORING AGENCY REPORT NUMBER	
11. SUPPLEMENTARY NOTES				
12a. DISTRIBUTION / AVAILABILITY STATEMENT Approved for public release, distribution is unlimited			12b. DISTRIBUTION CODE	
13. ABSTRACT (Maximum 200 words) A model for the short surface wave spectrum is presented, which includes the effects of wind forcing, surfactant damping, wave-current interactions, and wave breaking. A new analytical solution of the wave action equation was developed in order to account for wave-current interactions. The wave breaking model is based on a threshold criterion involving the vertical acceleration. The breaking fraction is then calculated as a function of the slope variance, and the backscatter is calculated from the Kirchhoff model by assuming a Gaussian correlation function within the breaking regions. Model predictions are compared with synthetic aperture radar observation made during the ONR/NRL High Resolution field experiment.				
14. SUBJECT TERMS Ocean Waves, Fronts, Radar Backscatter, Breaking Waves, Synthetic Aperture Radar			15. NUMBER OF PAGES 76	
			16. PRICE CODE	
17. SECURITY CLASSIFICATION OF REPORT Unclassified	18. SECURITY CLASSIFICATION OF THIS PAGE Unclassified	19. SECURITY CLASSIFICATION OF ABSTRACT Unclassified	20. LIMITATION OF ABSTRACT Unlimited	

CONTENTS

LIST OF FIGURES	v
1.0 INTRODUCTION	1
2.0 WAVE SPECTRUM MODELING	3
2.1. NET SOURCE FUNCTION	3
2.2. WAVE-CURRENT INTERACTIONS	9
2.3. SURFACTANT EFFECTS	11
2.4. ATMOSPHERIC STABILITY EFFECTS	13
2.5. WAVE BREAKING EFFECTS	13
3.0 RADAR BACKSCATTER MODELING	23
3.1. KIRCHHOFF APPROXIMATION	23
3.2. TWO-SCALE MODEL	25
3.3. BACKSCATTER FROM BREAKING WAVES	26
4.0 MODEL VALIDATION STUDIES	35
4.1. DOPPLER RADAR MEASUREMENTS	36
4.2. SAR DATA ANALYSIS	43
5.0 SUMMARY AND CONCLUSIONS	55
6.0 REFERENCES	57
APPENDIX	61

Accession For	
NTIS GRA&I	<input checked="" type="checkbox"/>
DTIC TAB	<input type="checkbox"/>
Unannounced	<input type="checkbox"/>
Justification	
By	
Distribution/	
Availability Codes	
Dist	Avail and/or Special
A-1	

LIST OF FIGURES

1.	Equilibrium Wave Height Spectrum $S(k, \phi)$ for Wind Speeds of 5 m/s and 10 m/s Calculated From Spectral Balance Model Using Plant's Growth Rate, With $\gamma=1$	7
2.	Comparison of Slope Variances Calculated From Spectral Balance Model With Measurements by Cox and Munk (1954)	8
3.	Contour Plot of the Change in the Curvature Spectrum, i.e. $k^4 S(k, \phi) - k^4 S_o(k, \phi)$, for a Converging Current	10
4.	Viscous Damping Rate for a Clean Water Surface and for a Surface Covered With a Monomolecular Layer of Oleyl Alcohol	12
5.	Equilibrium Wave Spectrum Calculated From Spectral Balance Model for Clean Water and for a Surface Covered With Oleyl Alcohol Monolayer	14
6.	Equilibrium Wave Spectrum for Unstable ($T_a - T_w < 0$) and Stable ($T_a - T_w > 0$) Conditions	15
7.	Breaking Fraction Versus Slope Variance, Using -0.4g Vertical Acceleration Threshold	18
8.	Breaking Fraction Versus Wind Speed, Using the Relationship Between Slope Variance and Wind Speed Observed by Cox and Munk (1954) for a Slick Surface	19
9.	Radar Cross Section Versus Large-Scale Slope Variance Calculated From Two Versions of the Two-Scale Model, for Vertical Polarization at 45° Incidence	27
10.	Radar Cross Section Versus Large-Scale Slope Variance Calculated From Two Versions of the Two-Scale Model, for Horizontal Polarization at 45° Incidence	28
11.	Comparison of X-Band Radar Backscatter Cross Sections Calculated From Kirchhoff and SPM Models for Surface Described by a Gaussian Correlation Function With rms Height and Correlation Length Both Equal to 0.5 cm . .	32

LIST OF FIGURES (CONTINUED)

12.	Comparison of Model Predictions (Dashed Line) With Measurements by Jessup <i>et al</i> (1991b) of Breaking Wave Contributions to the Average Radar Cross Section of the Ocean Surface	34
13.	Schematic Diagram of Doppler Radar. Gunn Diode Source is on the Left	37
14.	Photograph of Doppler Radar Mounted on the LADAS Platform. Radar is on the Near Side of the Mast, Next to Video Camera	40
15.	Examples of Doppler Radar In-Phase and Quadrature Signals Recorded During the High Resolution Field Experiment	41
16.	Plot of Doppler Spectrum Versus Time, Obtained From Radar Signals Recorded on September 16, 1991	42
17.	Backscattered Power Received by Doppler Radar on September 17, 1991 During a Crossing of the 'Rip' Feature	44
18.	Location of P3 SAR Data Set 1 (Pass 2) Relative to Bartlett Track From 10:00 to 12:00 EDT on September 16, 1991	46
19.	L-Band and X-Band Images for Subset Indicated in Figure 18. Horizontal Line Through L-Band Image is the "Double-Nadir" Return Which Occurs at an Incidence Angle of 60°	47
20.	L-Band Radar Cross Section Variations Across 'Rip' Current Feature, Calculated From Wave-Current Interaction Model Combined With Two-Scale Radar Backscatter Model	50
21.	X-Band Radar Cross Section Variations Across 'Rip' Current Feature, Calculated From Two-Scale Model (Solid Line) and Breaking Wave Model (Dashed Line)	51
22.	Slope Variances Calculated From Wave-Current Interaction Model for 'Rip' Feature	52

LIST OF FIGURES (CONCLUDED)

- 23. L-Band Image Signals Taken From a Vertical Cut Through
the Right-Hand Side of Image Shown in Figure 19 53
- 24. X-Band Image Signals Taken From a Vertical Cut Through
the Right-Hand Side of Image Shown in Figure 19 54

1.0 INTRODUCTION

This report summarizes the tasks completed and results obtained during the period 1 February 1990 to 31 January 1993 under ONR contract number N00014-90-C-0071. The overall goal of this research has been to contribute to a better understanding of the processes which cause variations in the radar backscatter from the ocean surface on scales of 1 meter to 1 kilometer, in order to enhance the utility of radar remote sensing techniques for oceanographic purposes. The specific objectives were to (1) develop a statistical model for the ocean surface which includes the effects of all the relevant processes which influence the small-scale surface roughness, (2) combine this model with an appropriate electromagnetic scattering model, and (3) test the predictions of the combined model using empirical data from laboratory and field experiments.

During the first year of this project, work centered on the theory of wave-current interactions using the wave action spectral transport equation. This task included both the development and exercise of models in order to make pre-experiment predictions for the High Resolution field experiment. The work resulted in the publication of a paper in the *Journal of Geophysical Research*, a copy of which is included as Appendix A of this report. Additional efforts under this task which have not been published in the open literature are described in section 2 of this report.

Subsequent modeling efforts included consideration of the radar backscatter problem, including a comparison of two implementations of the two-scale or composite model and an exploration of a new scattering model for breaking waves based on the Kirchhoff approximation. The results of this effort are described in section 3 of this report.

During the second and third years of this project, model verification studies were carried out using data collected during the High Resolution pilot experiment

which took place in September, 1991. A Doppler radar was deployed on the LADAS platform during this experiment, and data from this instrument was analyzed and compared with other measurements made during the experiment. Synthetic Aperture Radar data collected by the ERIM/NAWC P3 SAR system during the High Resolution experiment was also analyzed during the final year of this project. These efforts are described in section 4 of this report. Finally, a summary of the work accomplished and results obtained during this project is given in section 5.

2.0 WAVE SPECTRUM MODELING

The ocean surface may be described statistically in terms of the wave height spectrum $S(k, \phi)$ where k is the wavenumber and ϕ is the propagation direction. Although this description does not necessarily imply anything about the dynamics of the surface, the assumption is commonly made that the Fourier components which make up the spectrum may be regarded as freely propagating, linear surface waves. Spatial variations in the spectrum are then considered to be due to interactions of these waves with variable surface currents, surfactants, the atmosphere, and other waves.

The interaction of short waves with surface currents was investigated during the first year of this project using the wave action equation, and the results were published in the paper reproduced in Appendix A. Subsequently, further work was done on the net source function which appears on the right-hand side of this equation. Some of this work was presented orally at the Spring 1991 AGU meeting, but since it has not been published in printed form it is described in more detail in the following section.

2.1. NET SOURCE FUNCTION

The primary energy source for ocean surface waves is the atmosphere. Although the mechanisms responsible for the transfer of energy from the atmosphere are not entirely understood, they may be considered to fall into two categories. The initial formation of waves from a calm surface is thought to be caused by turbulent atmospheric pressure fluctuations which move across the water surface at the same speed as the waves (Phillips, 1957). The energy input due to this mechanism is denoted here by the function $\alpha(k, \phi)$. Once waves of a certain amplitude are present a feedback mechanism begins, leading to an exponential wave growth. The

rate of energy input due to this mechanism is therefore proportional to the spectral energy density, with a constant of proportionality denoted by $\beta(k, \phi)$.

Measurements of this quantity exhibit a large amount of scatter, but the expression

$$\beta_s = 0.25 \frac{\rho_a}{\rho_w} \left[\frac{U}{c} \cos(\phi - \phi_w) - 1 \right] \omega$$

given by Snyder *et al* (1981) is widely accepted for wavenumbers near the spectral peak, while the expression

$$\beta_p = 0.04 \left(\frac{u_*}{c} \right)^2 \omega \cos(\phi - \phi_w) \quad \text{for } |\phi - \phi_w| < \pi/2$$

suggested by Plant (1982) is generally considered to be valid at higher wavenumbers. Here U is the wind speed at 5 meters above the surface, u_* is the friction velocity (see section 2.4 below), c is the phase velocity and ω is frequency of the waves, ϕ is the wave propagation direction, ϕ_w the wind direction, and ρ_a and ρ_w are the densities of air and water, respectively.

In order for the wave system to reach a state of equilibrium, there must exist energy dissipation mechanisms which balance the energy input from the atmosphere. One such mechanism is due to the viscosity of the water. The rate of energy dissipation due to viscosity is given by $4\nu k^2$ times the spectral energy density, where ν is the kinematic viscosity of the water. However, this mechanism is capable of producing an equilibrium state only if $4\nu k^2 > \beta$, which occurs only at very high wavenumbers or very low wind speeds. Mathematically, a state of equilibrium can be produced by introducing a rate of dissipation which is a nonlinear functional of the energy spectrum. The simplest such term would be proportional to the spectral density raised to some power $n > 1$. For $n=2$ the net source function can be written as

$$\frac{dS}{dt} = \alpha + (\beta - 4\nu k^2) S - \gamma \omega k^4 S^2$$

where γ is a dimensionless constant. The steady-state solution of this equation yields the equilibrium spectrum

$$S_o(k, \phi) = \frac{\beta - 4\nu k^2 + \sqrt{(\beta - 4\nu k^2)^2 + 4\alpha\gamma\omega k^4}}{2\gamma\omega k^4}.$$

Although the form and magnitude of the Phillips growth term is uncertain, it is assumed to be the dominant term for wavenumbers near the spectral peak. In this region, the equilibrium spectrum is then given by approximately

$$S_o(k, \phi) \approx \left(\frac{\alpha}{\gamma\omega k^4} \right)^{1/2}.$$

It is further assumed that in this region the equilibrium spectrum has the form given by Pierson and Moskowitz (1964). This would imply that the Phillips or linear growth term can be written as

$$\alpha = \gamma\omega k^4 S_{PM}^2(k, \phi)$$

where $S_{PM}(k, \phi)$ is the Pierson-Moskowitz spectrum converted into wavenumber space, i.e.

$$S_{PM}(k, \phi) = 0.0081 g^2 \omega^{-5} e^{-0.74(\omega_o/\omega)^4} F(\phi) \frac{1}{k} \frac{d\omega}{dk}$$

where g is the gravitational acceleration, $\omega_o = g/U$, U is the wind speed at 19.5 meters above the surface, $F(\phi)$ is an angular distribution function such as

$$F(\phi) = \frac{4}{3\pi} \cos^4\left(\frac{\phi - \phi_w}{2}\right)$$

and ω is given by the dispersion relation

$$\omega^2 = gk + \frac{\tau}{\rho} k^3$$

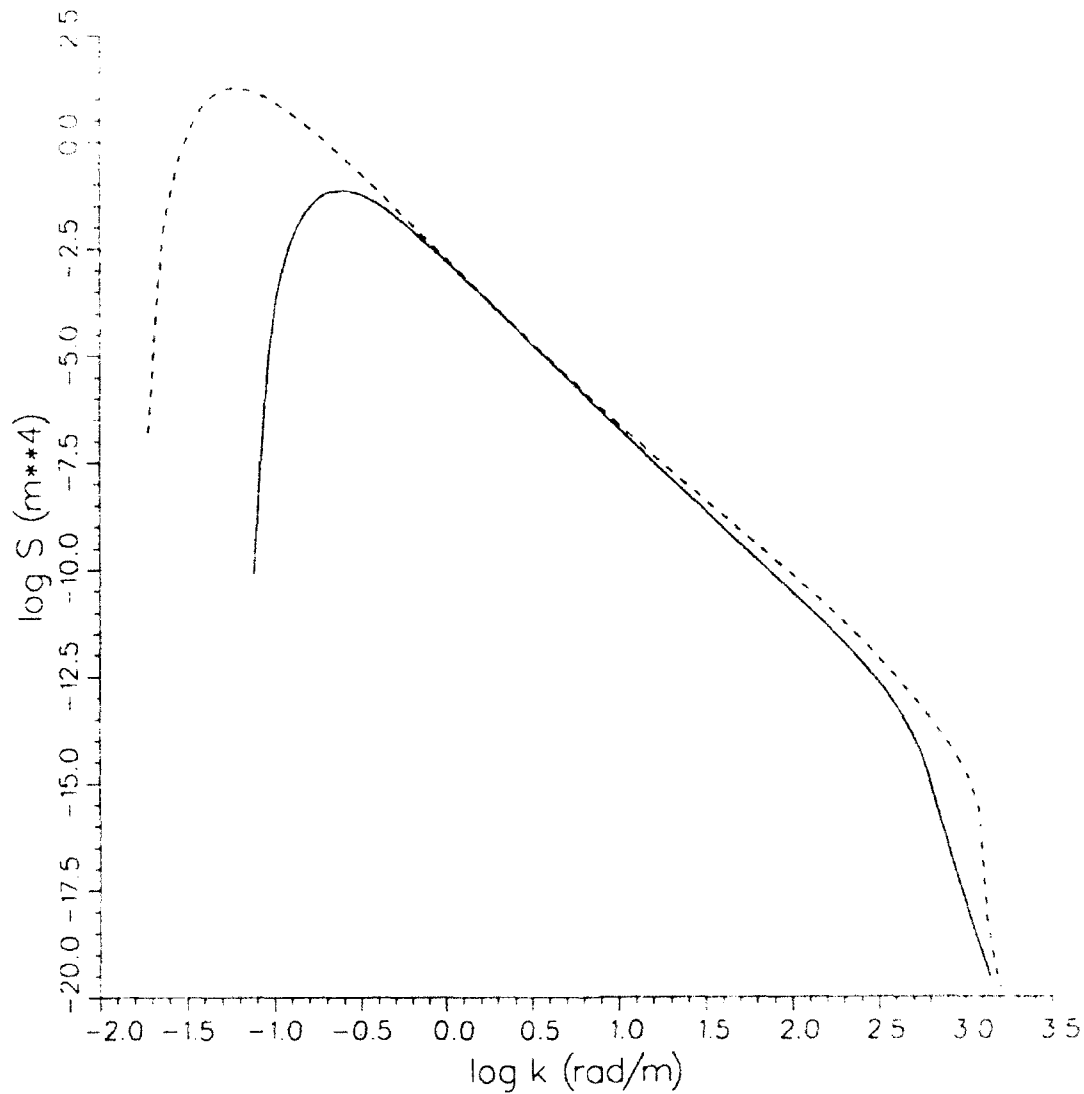
where τ is the surface tension and ρ is the density of water.

At high wavenumbers, where the viscous dissipation term dominates, the equilibrium spectrum approaches

$$S_o(k, \phi) \approx \frac{\alpha}{4\nu k^2}$$

which falls off as k^{-10} for $k^2 \gg \rho g / \tau$. The range of wavenumbers where this approximation holds is sometimes referred to as the viscous cutoff region.

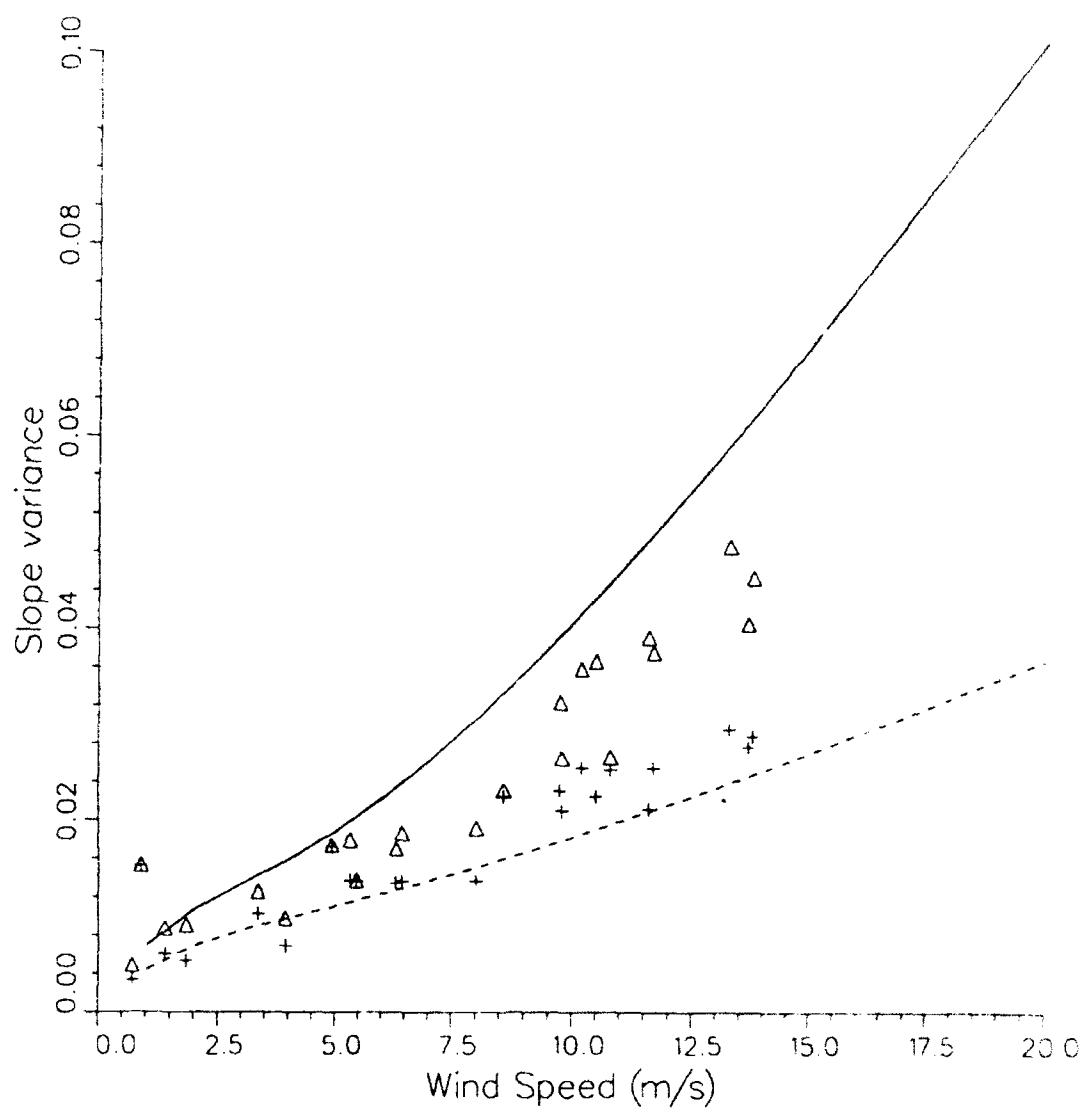
At intermediate wavenumbers, the exponential growth term dominates and the equilibrium spectrum predicted by this model is larger than the Pierson-Moskowitz spectrum. The amount of this enhancement depends on the wind speed and also on the value of the constant γ . An example plot of the equilibrium wave height spectrum for $\gamma=1$, using the growth rate suggested by Plant (1982), is shown in Figure 1. The wavenumber dependence shown here is qualitatively similar to that suggested by Pierson and Stacy (1973) and Bjerkaas and Riedel (1979). However, the detailed structure shown in the measurements by Jähne and Riemer (1990) is not accounted for by this model (see sections 2.5 and 4.2 below). Multiplying the height spectrum by $k^2 \cos^2(\phi - \phi_w)$ and $k^2 \sin^2(\phi - \phi_w)$ and integrating over all wavenumbers yields the slope variances in the upwind and crosswind directions, respectively, as shown in Figure 2. These slope variances agree fairly well with those measured by Cox and Munk (1954) which are also shown in Figure 2.



LEGEND

Wind Speed = 5 m/s	_____
Wind Speed = 10 m/s	-----

Figure 1. Equilibrium Wave Height Spectrum $S(k, \phi)$ for Wind Speeds of 5 m/s and 10 m/s Calculated From Spectral Balance Model Using Plant's Growth Rate, With $\gamma=1$.



LEGEND

Up-wind component

Cross-wind component

△ Cox & Munk data (upwind)

+ Cox & Munk data (crosswind)

Figure 2. Comparison of Slope Variances Calculated From Spectral Balance Model With Measurements by Cox and Munk (1954).

2.2. WAVE-CURRENT INTERACTIONS

The net source function discussed in the previous section can be rewritten in terms of the action spectral density $N(k, \phi) = \rho c S(k, \phi)$ as

$$\frac{dN}{dt} = \alpha' + (\beta - 4\nu k^2) N - \gamma' \omega k^4 N^2$$

where $\alpha' = \rho c \alpha$ and $\gamma' = \gamma / \rho c$. This equation can be used, along with the ray equations

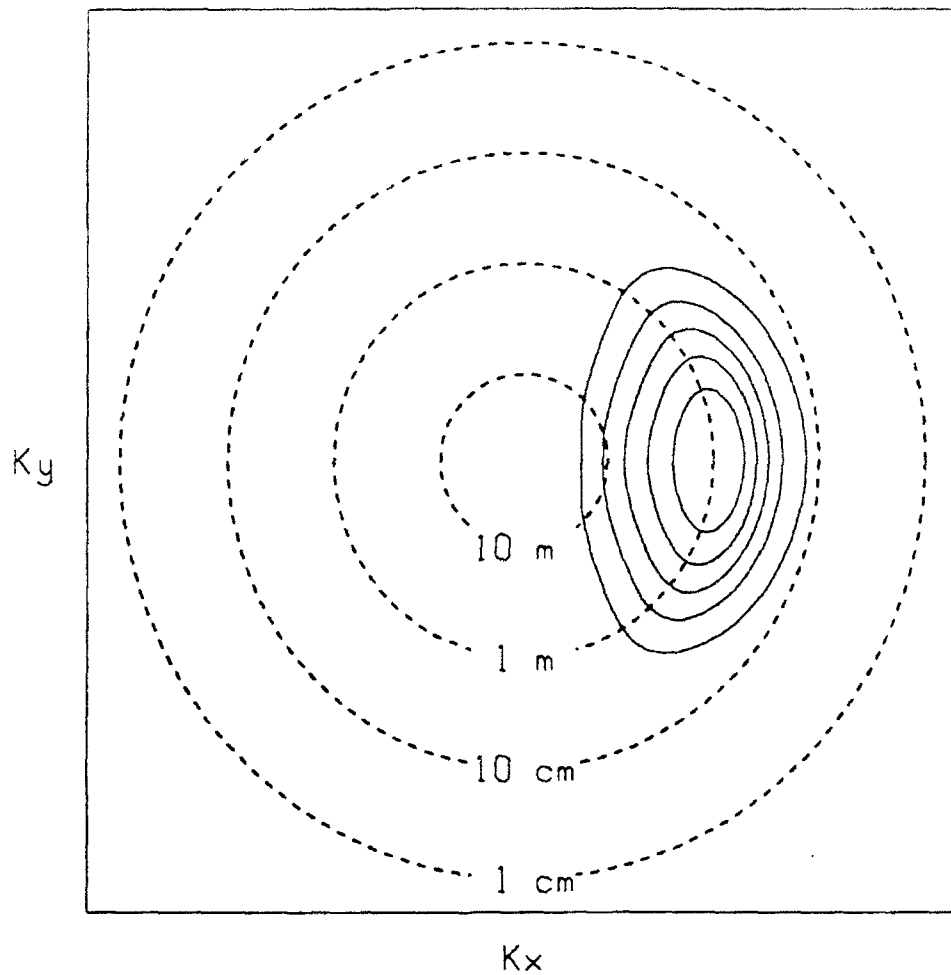
$$\begin{aligned} \frac{dx}{dt} &= c_{gx} + u & \frac{dk_x}{dt} &= -k_x \frac{\partial u}{\partial x} - k_y \frac{\partial v}{\partial x} \\ \frac{dy}{dt} &= c_{gy} + v & \frac{dk_y}{dt} &= -k_x \frac{\partial u}{\partial y} - k_y \frac{\partial v}{\partial y} \end{aligned}$$

to calculate the evolution of a wave packet as it interacts with a variable surface current. Alternatively, these five equations can be combined into a single partial differential equation as discussed in Lyzenga and Bennett (1988). The paper reproduced in Appendix A discusses an analytic solution of this equation, obtained by approximating the net source function by $-\beta_r (N - N_0)$ where N_0 is the equilibrium action spectrum and β_r is a relaxation rate. Using a Taylor expansion of the net source function described above, this relaxation rate may be written as

$$\beta_r = \sqrt{(\beta - 4\nu k^2)^2 + 4\alpha\gamma\omega k^4}.$$

Note that $\beta_r \approx \beta$ in the intermediate wavenumber range where the exponential growth term dominates, and $\beta_r \approx 4\nu k^2$ in the viscous cutoff region.

An example calculation of the change in the wave spectrum due to a converging current is shown in Figure 3. Additional examples are discussed in Appendix A and in section 4.2 below. A general characteristic of these calculations is that the maximum effects are predicted at wavelengths on the order of 1 meter, and



$$\left(\frac{du}{dx}\right) = -0.01 \text{ sec}^{-1} \quad \left(\frac{dv}{dx}\right) = 0$$

$$w = 100 \text{ m} \quad U = 5 \text{ m/s} \rightarrow$$

Figure 3. Contour Plot of the Change in the Curvature Spectrum, i.e. $k^4 S(k, \phi) - k^4 S_o(k, \phi)$, for a Converging Current. Fractional Change in the Spectral Density is on the Order of Unity at $\lambda=1\text{ m}$ and One Percent at $\lambda=1\text{ cm}$ (Note Logarithmic Wavenumber Scale).

very small changes in the wave spectrum are predicted at wavelengths of less than 10 cm. These predictions are apparently at odds with the observation of large changes in microwave backscatter associated with current gradients on the ocean surface, since the microwave backscatter is generally considered to be governed by the surface wave spectral density at wavelengths comparable to the radar wavelength. The studies discussed in the remainder of this report were motivated in large part by this apparent discrepancy. A more quantitative evaluation of the accuracy of the predictive models will be presented in section 4 below.

2.3. SURFACTANT EFFECTS

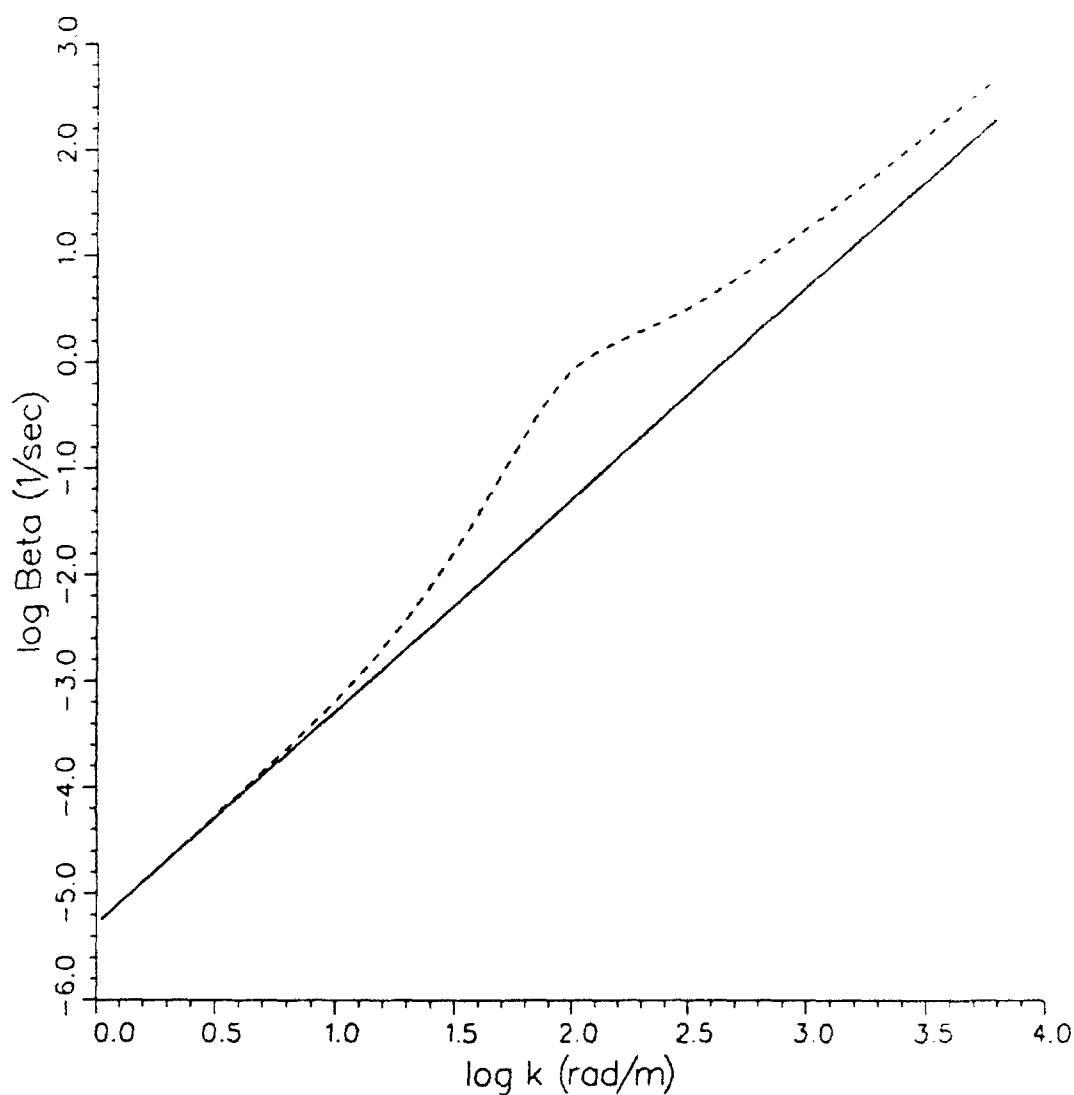
The viscous damping of surface waves is enhanced by the presence of surfactant films. A linearized theory of this damping effect was developed by Dorrestein (1951) and Levich (1962). Empirical validation of this theory was provided by Cini and Lombardini (1981). The main parameter influencing the amount of wave damping is the surface elasticity E which describes the change in surface tension upon compression of the film. Diffusion or adsorption effects can be incorporated by considering this to be a complex quantity. However, in the simpler case in which the elasticity is real, the surface wave damping rate is given by

$$\beta_d = 4\nu k^2 \frac{1 - X + XY}{1 - 2X + 2X^2}$$

where

$$X = \frac{Ek^2}{\rho\omega\sqrt{2\nu\omega}} \quad \text{and} \quad Y = \frac{Ek}{4\rho\nu\omega}$$

(Cini *et al.*, 1987). Figure 4 shows a plot of the viscous damping rate for a clean surface ($E=0$) and for a surface covered with oleyl alcohol, which has an elasticity $E=22.5$ dyne/cm. The damping rate for the film-covered surface has a characteristic



LEGEND
clean surface
 Elasticity = 22.5 mN/m

Figure 4. Viscous Damping Rate for a Clean Water Surface and for a Surface Covered With a Monomolecular Layer of Oleyl Alcohol.

peak at a wavenumber of about 2 rad/cm, which is caused by a resonant coupling of the surface wave energy into longitudinal or Marangoni waves within the surface film.

This damping rate can be used in the net source function, as discussed in Section 2.1, in order to determine the change in the equilibrium spectrum due to the presence of a surface film. Example results of such a calculation are shown in Figure 5 for an oleyl alcohol film.

2.4. ATMOSPHERIC STABILITY EFFECTS

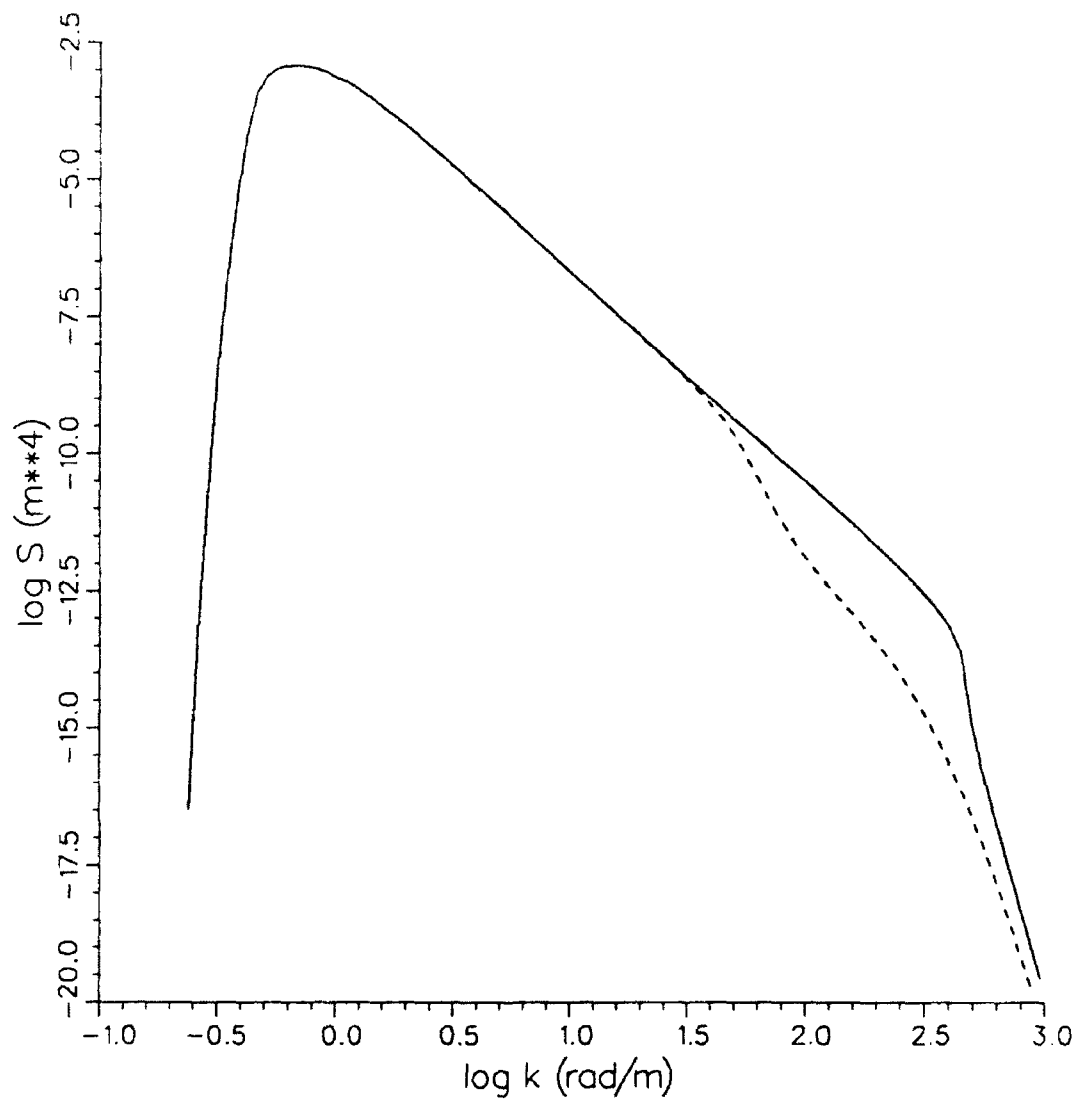
The wind-wave growth rate introduced by Plant (1982) involves the friction velocity $u_* = \sqrt{\tau/\rho}$ where τ is the wind stress and ρ is the density of air. The wind stress is dependent on atmospheric stability conditions as well as the wind speed. An empirical relationship among these variables, as determined from a set of 214 records over a range of windspeeds from 2 to 21 m/sec (Geernaert, 1990), can be written as

$$u_*^2 = (2.58 U + 0.49 U^2 + 0.07 U^3 - 1.06 \Delta T) \times 10^{-3} \text{ m}^2/\text{sec}^2$$

where U is the windspeed (in m/sec) measured at 10 m above the surface and ΔT is the difference between the air and water temperatures (in °C). Using this relationship to calculate the growth rate, and solving for the equilibrium spectrum as discussed in section 2.1, yields the results shown in Figure 6 for $U=3$ m/sec and two values of ΔT corresponding to stable ($\Delta T > 0$) and unstable ($\Delta T < 0$) conditions. Note that the largest effects are predicted at very short wavelengths.

2.5. WAVE BREAKING EFFECTS

The net source function discussed in section 2.1 includes a dissipation term which is thought to be due primarily to the effects of wave breaking (Phillips, 1977, 1985). However, it does not incorporate any corresponding source of wave energy or spectral density. There is ample empirical evidence that small-scale roughness is

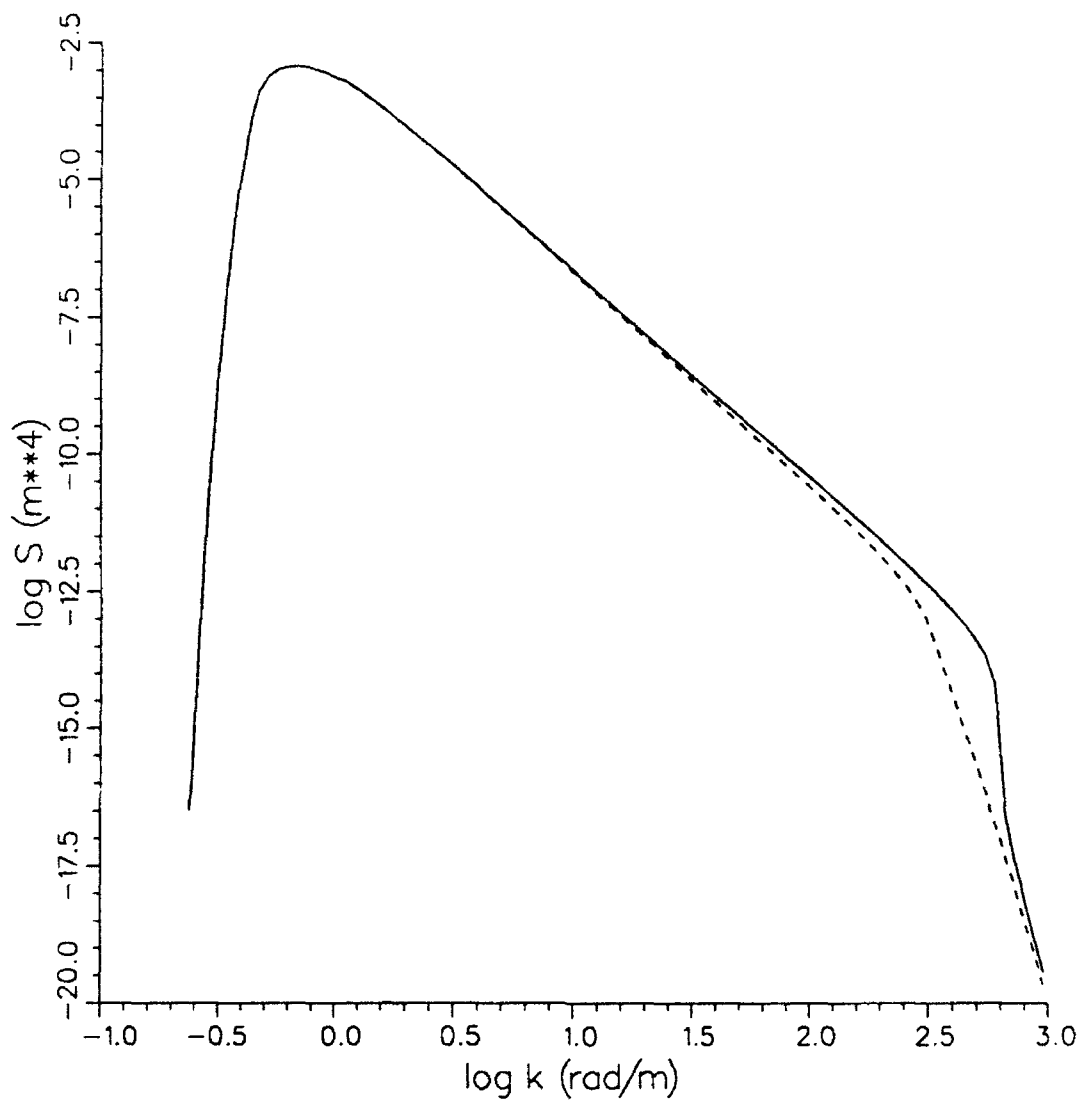


LEGEND

U= 3.0 m/s, Td= 0.0 C, E= 0.0 mN/m

--- U= 3.0 m/s, Td= 0.0 C, E= 22.5 mN/m ---

Figure 5. Equilibrium Wave Spectrum Calculated From Spectral Balance Model for Clean Water and for a Surface Covered With Oleyl Alcohol Monolayer.



LEGEND

U= 3.0 m/s, Td= -5.0 C, E= 0.0 mN/m

--- U= 3.0 m/s, Td= 5.0 C, E= 0.0 mN/m ---

Figure 6. Equilibrium Wave Spectrum for Unstable ($T_a - T_w < 0$) and Stable ($T_a - T_w > 0$) Conditions.

generated by breaking waves (e.g. Banner and Fooks, 1985), although there is considerable uncertainty as to the details of this process. This section describes a first attempt to model the effects of wave breaking on the surface roughness. The effects of this change in roughness on the radar backscatter are considered in section 3.3 below.

A procedure for predicting the fraction of the surface covered by breaking wave crests has been developed and to some extent validated by several authors. The procedure assumes that there is a threshold on the downward vertical acceleration at the surface of the water, beyond which the surface becomes unstable and breaks. A breaking threshold of $-g/2$ was suggested by Longuet-Higgins (1969), this being the limiting acceleration near the crest of a Stokes wave. Laboratory observations of wave breaking by Ochi and Tsai (1983) were shown by Srokosz (1983) to be consistent with a threshold of $-\alpha g$, where $\alpha \approx 0.4$. Using this threshold and assuming that the values of the vertical acceleration are normally distributed with mean zero and standard deviation σ_a , as in Snyder and Kennedy (1983), the fraction of the surface covered by breaking water is given by

$$f_b = \int_{-\infty}^{-\alpha g} \frac{1}{\sqrt{2\pi}\sigma_a} \exp\left[-\frac{a_z^2}{2\sigma_a^2}\right] da_z = 0.5 \operatorname{erfc}\left(\frac{\alpha g}{\sqrt{2}\sigma_a}\right).$$

For gravity waves, the variance of the vertical acceleration is given by

$$\sigma_a^2 = \int_0^{\omega_c} \omega^4 S_\omega(\omega) d\omega = \int_0^{2\pi} \int_0^{k_c} g^2 k^2 S(k, \phi) k dk d\phi = g^2 \sigma_s^2$$

where σ_s^2 is the slope variance and k_c is a cutoff wavenumber which defines the

spatial scale of the breaking waves. A plot of the breaking fraction as a function of the slope variance is shown in Figure 7. The cutoff wavenumber is somewhat arbitrary, but for the present purposes it is assumed to lie near the boundary between gravity and capillary waves. The slope variance in this equation may therefore be associated with that measured by Cox and Munk (1954) in the presence of a surface slick, which would presumably damp out the capillary waves as discussed in section 2.3 above. The total (upwind plus crosswind) slope variance under these conditions was found to be related to the wind speed by the equation

$$\sigma_s^2 = \sigma_c^2 + \sigma_u^2 = 0.008 + 0.00156 W$$

where W is the wind speed (in m/sec) recorded at 41 feet above sea level. The fractional breaking area using this equation for the slope variance is plotted in Figure 8. For wind speeds between 3 and 15 m/s the breaking fraction is approximated quite closely by the equation

$$f_b \approx 0.0044 \left(\frac{W}{10} \right)^{2.57} \quad 3 < W < 15 \text{ m/s.}$$

This is roughly half of the fractional whitecap coverage as given by Spillane *et al* (1986), although it is somewhat closer to the observations of Kondo *et al* (1973).

Given the foregoing macroscopic description of the surface in terms of the breaking fraction f_b , the next step is to attempt to statistically describe the microstructure within the breaking regions. Here we are faced with the problem that wave breaking may encompass a wide variety of phenomena, ranging from parasitic capillary generation at the onset of small-scale breaking to the formation of droplets, bubbles, and foam during the most energetic large-scale breaking events. Although the latter cases are the most obvious and easily observed, the breaking criterion discussed above suggests that a large fraction of the breaking surface area may be associated with relatively short waves. For a k^{-4} spectrum, the slope variance within

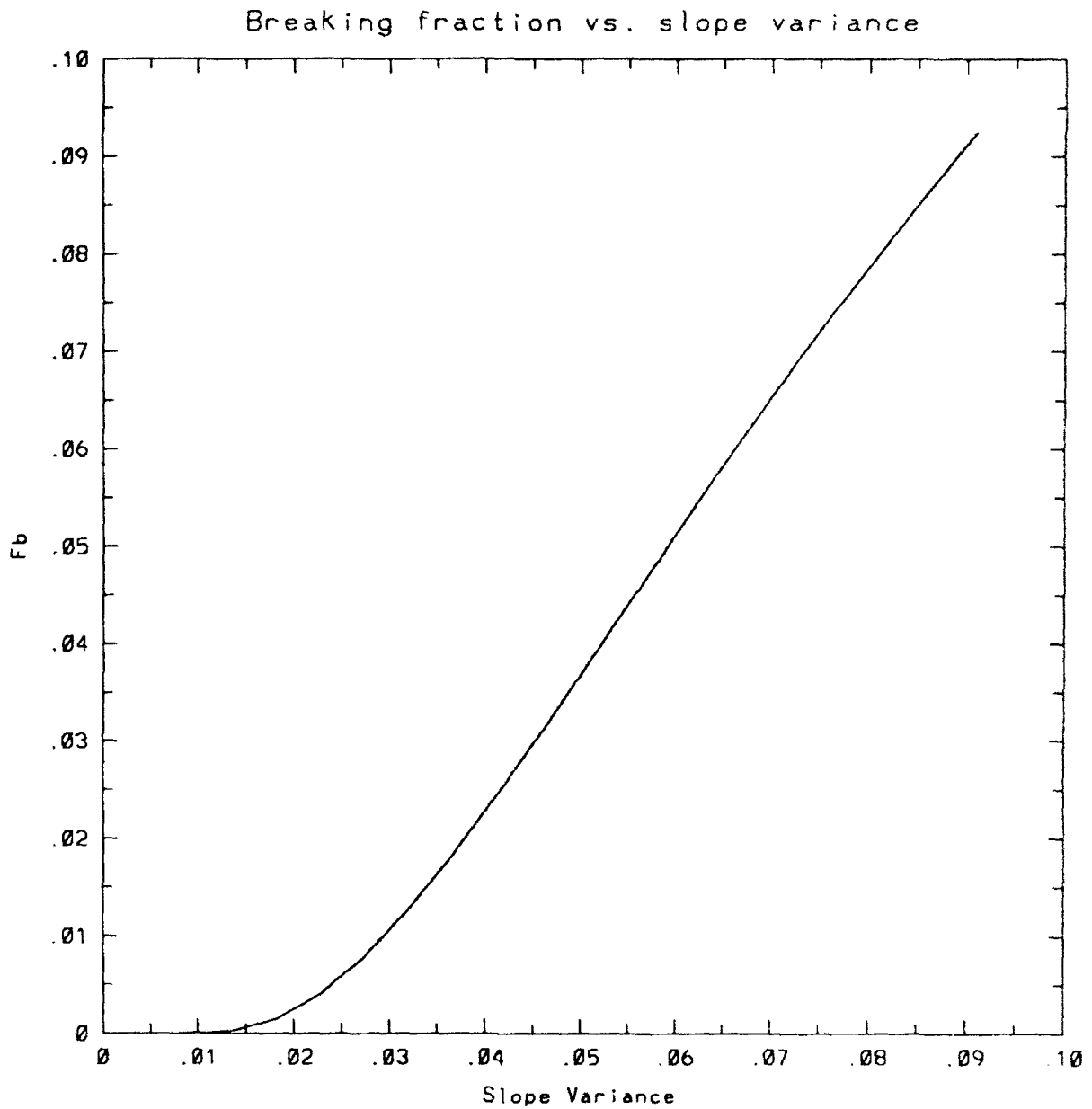


Figure 7. Breaking Fraction Versus Slope Variance, Using $-0.4g$ Vertical Acceleration Threshold.

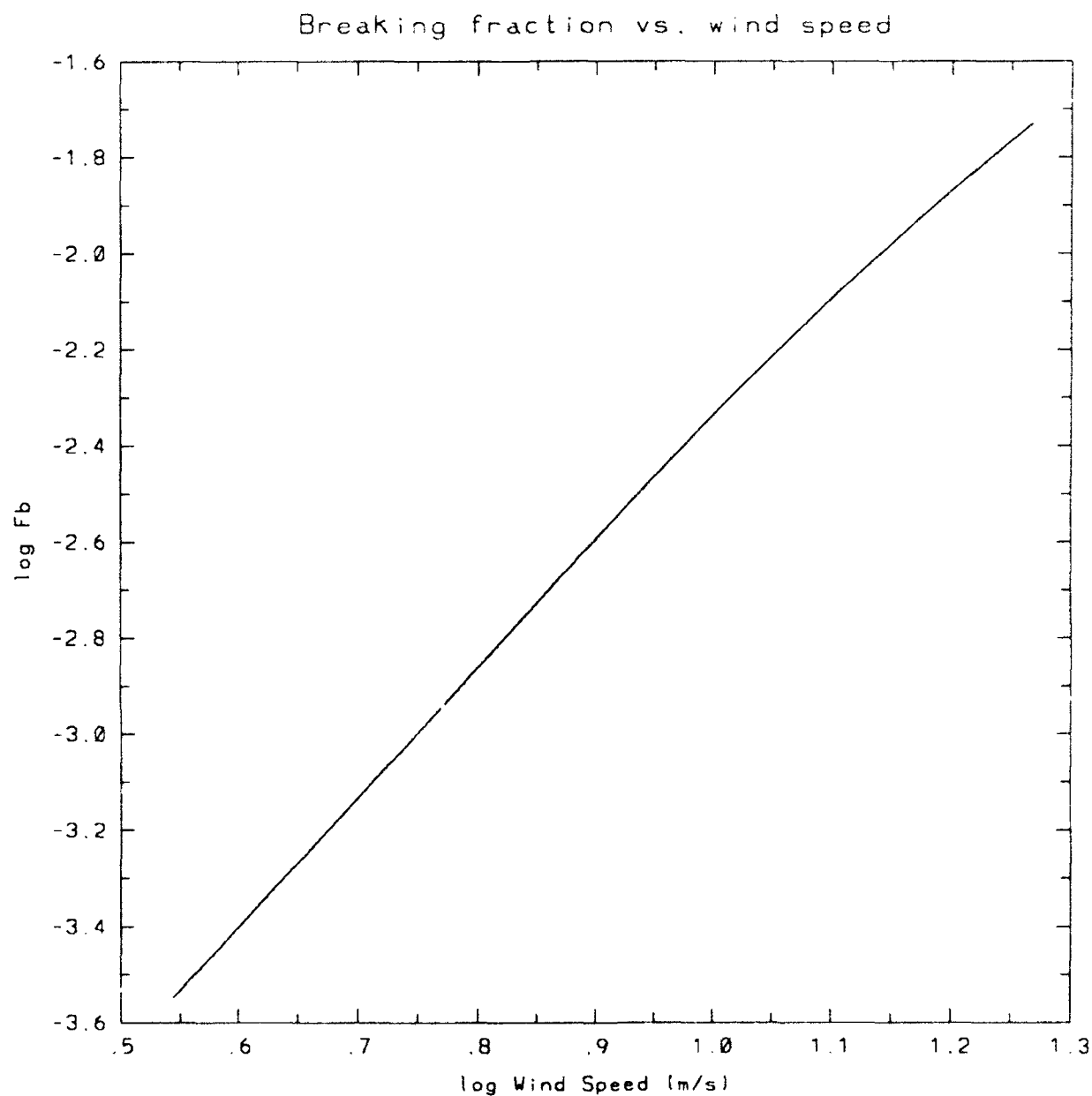


Figure 8. Breaking Fraction Versus Wind Speed, Using the Relationship Between Slope Variance and Wind Speed Observed by Cox and Munk (1954) for a Slick Surface.

the wavenumber interval from k_1 to k_2 is proportional to $\ln(k_2/k_1)$. Thus, for example, wavelengths from 10 cm to 1 meter contribute the same amount as wavelengths from 1 to 10 meters. Therefore, features associated with small-scale breaking waves, such as parasitic capillary wave generation, may be as important as large-scale breaking events for the purposes considered here.

Laboratory measurements by Banner and Fooks (1985) indicate that the roughness generated by 20-30 cm breaking waves is fairly narrow-banded. Field measurements by Kondo *et al* (1973) associated breaking waves with local increases in the height variance calculated over time intervals of 0.2 sec. Typical values of the r.m.s. surface height for these high-frequency components were on the order of 0.5-1 cm in the presence of breaking waves. Values of this r.m.s. height were also calculated for all observations (with and without breaking) and plotted versus the wind speed.

For a given measurement interval, the height variance associated with the roughness caused by wave breaking may be assumed to be proportional to the fraction of the surface covered by breaking water during this interval, and may be written as

$$\overline{h_b^2} = f_b h_b^2$$

where h_b^2 is the height variance within the breaking regions. The spatial structure of both breaking and non-breaking regions can be described by means of the autocovariance function

$$\phi(\mathbf{r}) = \langle \eta(\mathbf{r}') \eta(\mathbf{r}'+\mathbf{r}) \rangle$$

where $\eta(\mathbf{r})$ is the surface height and the brackets indicate ensemble averages. It will be assumed here that the surface within a breaking region may be characterized by a covariance function having a correlation length r_c which is much smaller than the correlation length in the absence of breaking.

Assuming the small-scale height variations within the breaking regions are uncorrelated with the larger-scale height variations on the underlying surface, the total height autocovariance function can be written as

$$\phi(\mathbf{r}) = \phi_b(\mathbf{r}) + \phi_{nb}(\mathbf{r}) .$$

It is further assumed that the shape of the breaking wave contribution to the covariance function is approximately gaussian and isotropic, and can thus be written as

$$\phi_b(\mathbf{r}) = f_b h_b^2 e^{-r^2/r_c^2}$$

where r_c is the correlation length within the breaking region.

Using this expression for the surface height autocovariance function, the corresponding height spectrum can be written as

$$\begin{aligned} S(k, \theta) &= \frac{1}{(2\pi)^2} \iint \phi(\mathbf{r}) e^{i k r \cos(\theta - \theta')} r dr d\theta' \\ &= \frac{f_b h_b^2}{2\pi} \int e^{-r^2/r_c^2} J_0(kr) r dr + S_{nb}(k, \theta) \\ &= \frac{1}{4\pi} f_b h_b^2 r_c^2 e^{-\frac{1}{4} k^2 r_c^2} + S_{nb}(k, \theta) . \end{aligned}$$

Detailed measurements of the short wavelength portion of the wave spectrum in a large wind wave facility have been made by Jähne and Riemer (1990). These measurements show a weak dependence of the spectrum on the wind speed or friction velocity at wavenumbers below 1 rad/cm and a much stronger dependence at higher wavenumbers, with a sharp cutoff in the spectrum at a wavenumber of approximately 8 rad/cm. The wind speed dependence for wavenumbers between 1 and 8 rad/cm and

friction velocities between about 10 and 50 cm/s is described as approximately a power law in the friction velocity, with an exponent between 2.5 and 3. For the lowest wind speeds the dimensionless curvature spectrum or "degree of saturation" $B(k)$, which is defined as k^4 times the height spectrum, falls off rapidly between wavenumbers of 1 and 2 rad/cm.

One possible interpretation of Jähne and Riemer's measurements is that for wavenumbers below 1 rad/cm, the spectrum results from a balance between the wind input and various dissipation mechanisms as discussed in section 2.1 above, whereas for larger wavenumbers the spectrum is dominated by wave breaking effects. Under this hypothesis, the rapid increase in the spectrum with wind speed at these wavenumbers is then due to the strong dependence of the breaking fraction f_b on the slope variance. The observed cutoff in the spectrum at 8 rad/cm is consistent with a value of r_c of roughly 0.5 cm. Furthermore, the observed spectral levels in the region of 1 to 8 rad/cm appear to be predicted fairly well by assuming a value of $h_b \approx r_c$ and using the breaking fraction calculated as described earlier in this section.

3.0 RADAR BACKSCATTER MODELING

The problem of predicting the statistics of the radar backscatter from the ocean surface is one of long standing. There are well-known solutions of this problem in the limiting cases where the electromagnetic wavelength is either much longer or much shorter than the relevant spatial scales of the surface roughness. However, for electromagnetic radiation in the microwave region of the spectrum, and at intermediate angles of incidence, the spatial scales for typical ocean surfaces are such that neither of these limiting solutions is valid.

The most widely accepted approximate solution within this intermediate scattering regime is the composite or two-scale model. Some problems associated with this model are discussed in section 3.2 below. An alternative approach is provided by the Kirchhoff or physical optics approximation. This approximation is reviewed in the following section, and is applied to the problem of breaking wave backscatter in section 3.3.

3.1. KIRCHHOFF APPROXIMATION

Electromagnetic radiation striking the surface of a highly conducting medium, such as the ocean, induces a surface current $\mathbf{J}_s(\mathbf{r})$. Once this current is known, the scattered magnetic field can be calculated from the equation

$$\mathbf{H}_s(\mathbf{r}) = \int \nabla G(\mathbf{r} - \mathbf{r}') \times \mathbf{J}_s(\mathbf{r}') d\mathbf{r}'$$

where

$$G(\mathbf{r} - \mathbf{r}') = \frac{e^{ik|\mathbf{r} - \mathbf{r}'|}}{4\pi|\mathbf{r} - \mathbf{r}'|}.$$

The Kirchhoff or physical optics approximation is obtained by assuming that the

surface current is given by

$$\mathbf{J}_s(\mathbf{r}) = 2\mathbf{n}(\mathbf{r}) \times \mathbf{H}_i(\mathbf{r})$$

where $\mathbf{n}(\mathbf{r})$ is the surface normal and $\mathbf{H}_i(\mathbf{r})$ is the incident magnetic field. This is equivalent to the current which would be present on an infinite flat plane tangent to the surface at the location \mathbf{r} . If the surface height $\eta(x, y)$ is assumed to be a Gaussian-distributed random variable, the radar cross section per unit area is then given by

$$\sigma_o = \frac{1}{\pi} k_o^2 \sec^2 \theta \iint \Gamma(x, y) e^{-2ik_h x} dx dy$$

where k_o is the radar wavenumber, θ is the incidence angle, $k_h = k_o \sin \theta$, $k_z = k_o \cos \theta$ and

$$\Gamma(x, y) = \exp \{ 4k_z^2 [\phi(x, y) - \phi(0, 0)] \}$$

where $\phi(x, y)$ is the surface height autocovariance function (Holliday *et al.*, 1986).

In the limit as $k_z \rightarrow \infty$, $\Gamma(x, y)$ is non-zero only in an infinitesimal region around the origin, over which the covariance function $\phi(x, y)$ can be expanded in a Taylor series to second order in x and y . The integral for σ_o can then be evaluated analytically to yield the well-known specular scattering result (Barrick, 1968). On the other hand, as $k_z \rightarrow 0$ the small-argument approximation can be used for the exponential function in the above equation, with the result that σ_o becomes proportional to the surface height spectral density at the "Bragg" wavenumber $k_B = 2k_h = 2k_o \sin \theta$. However, the constant of proportionality in the resulting expression is different from that obtained by the small perturbation method (SPM). It has been shown by Holliday (1987) that if a second iteration is performed by calculating the current induced by the first-order scattered field in the Kirchhoff

approximation, the SPM result is reproduced for both vertical and horizontal polarization.

It can be seen, therefore, that although the Kirchhoff approximation is inferior to the SPM in some respects, it has certain advantages in that it does not rely on the assumption that the waveheight is much smaller than the electromagnetic wavelength. This makes the approximation attractive for some cases, such as the one discussed in section 3.3, where the wave height may not be small enough for the SPM to be valid and for which the two-scale model is not applicable because the roughness is basically on a single length scale.

3.2. TWO-SCALE MODEL

There are several variations and several methods of deriving the two-scale model, but the basic idea is to apply the small perturbation or Bragg scattering model to small patches of the surface, each of these patches having a different slope or orientation with respect to the overall scattering surface. The total scattered power is then obtained by summing or integrating over all possible slopes of the Bragg scattering patches. There is some ambiguity regarding the scale separation wavelength, which influences the distribution of slopes included in the integration, and also regarding the method of performing this integration. In addition, the two-scale model makes certain assumptions about the surface height and slope statistics (namely, that they are uncorrelated) which may be violated at small scales and in the presence of wave breaking and parasitic capillary wave generation.

The radar cross section given by the two-scale model can be written in its simplest form as

$$\sigma_o = \iint \sigma_B(\eta_x, \eta_y) P(\eta_x, \eta_y) d\eta_x d\eta_y$$

where $\sigma_B(\eta_x, \eta_y)$ represents the Bragg scattering cross section per unit area for a

surface element having slope components η_x and η_y , and $P(\eta_x, \eta_y)$ represents the probability density function for these slopes. This integral can be evaluated numerically, using well-known expressions for the Bragg scattering cross section as described for example in Lyzenga and Bennett (1988). An example of the results for vertically and horizontally polarized radiation, assuming a k^{-4} short wave spectrum and a 45° incidence angle, are shown in Figures 9 and 10 as a function of the slope variance σ_s^2 .

Alternatively, the Bragg scattering cross section can be expanded as a Taylor series in the slopes η_x and η_y and the integration can be carried out analytically. In fact, it is argued by Plant (1986) that it is "inconsistent" to carry out this expansion beyond second order in the surface slope. This implies that the radar cross section is a linear function of the slope variance, as shown by the dashed lines in Figures 9 and 10. Obviously, there is a large difference between the results for horizontal polarization when the slope variance exceeds about 0.03, or the r.m.s. tilt angle exceeds 10° .

3.3. BACKSCATTER FROM BREAKING WAVES

Measurements of the X-band radar backscatter from breaking waves at near-grazing angles of incidence led Lewis and Olin (1980) to propose that breaking regions may be considered as perfect isotropic reflectors, with all of the incident energy being scattered uniformly throughout the upper hemisphere. This would imply a radar cross section per unit area on the order of unity, or more precisely

$$\sigma_o \approx 2 \cos \theta$$

where θ is the angle of incidence. Field measurements of microwave backscatter made at intermediate incidence angles have also been interpreted in terms of the contributions from wave breaking by Jessup et al (1990, 1991a, 1991b) as discussed

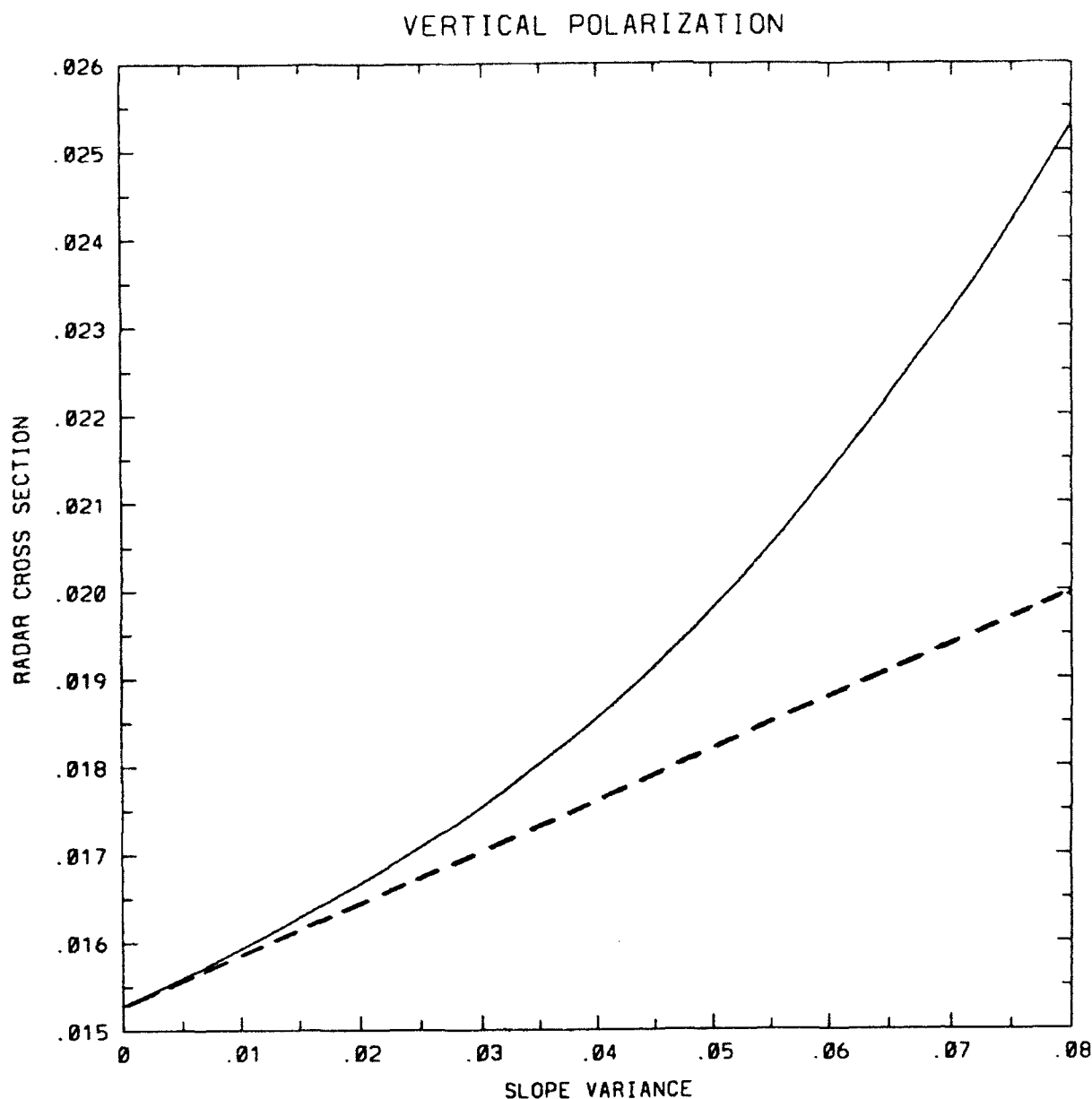


Figure 9. Radar Cross Section Versus Large-Scale Slope Variance Calculated From Two Versions of the Two-Scale Model, for Vertical Polarization at 45° Incidence. Solid Line Indicates Result of a Numerical Integration Over Wave Slopes, as Described by Lyzenga and Bennett (1988), and Dashed Line Indicates Analytical Result Obtained by Plant (1986).

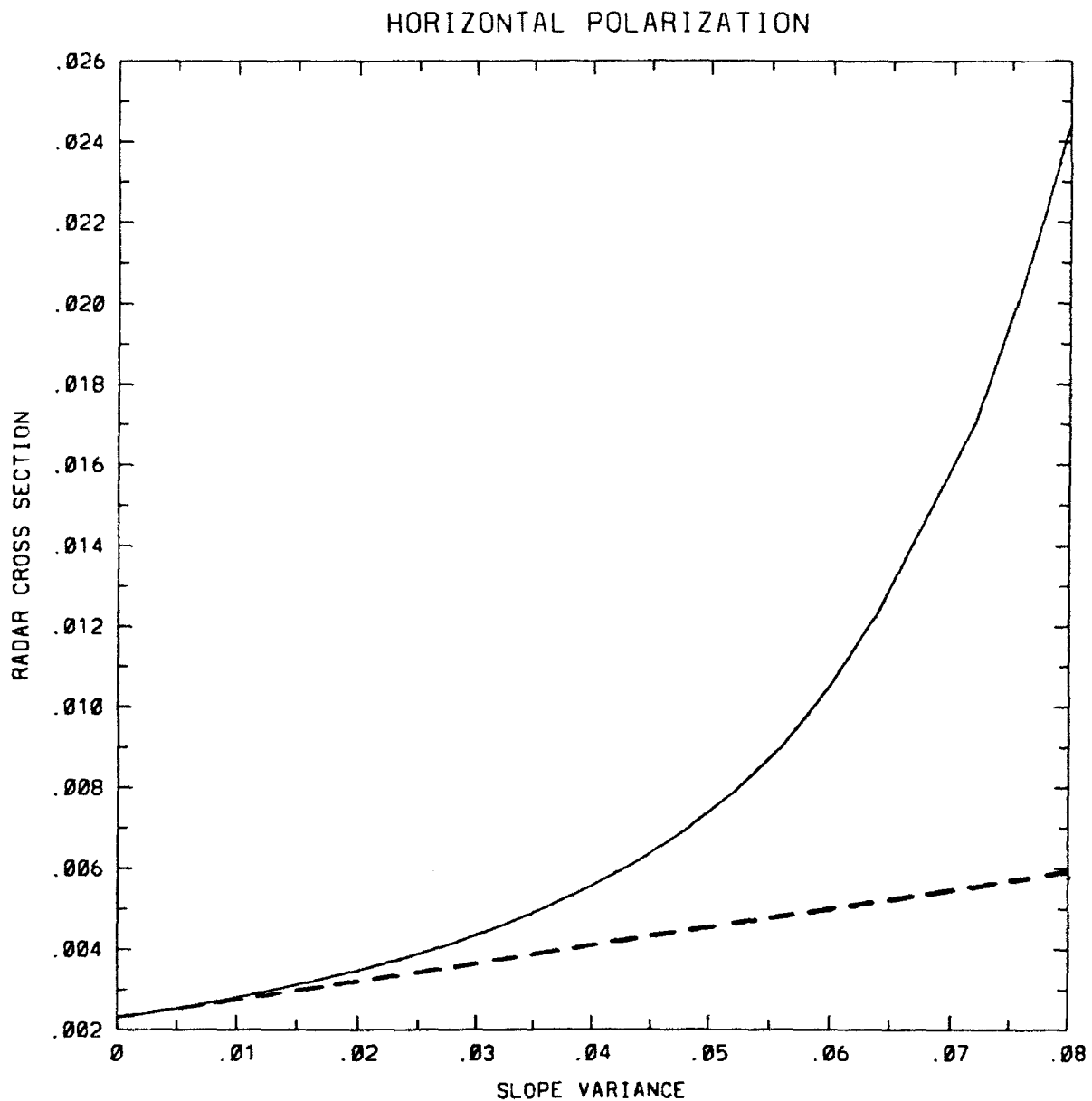


Figure 10. Radar Cross Section Versus Large-Scale Slope Variance Calculated From Two Versions of the Two-Scale Model, for Horizontal Polarization at 45° Incidence. Solid Line Indicates Result of a Numerical Integration Over Wave Slopes, as Described by Lyzenga and Bennett (1988), and Dashed Line Indicates Analytical Result Obtained by Plant (1986).

below. Additional laboratory measurements of the radar backscatter from breaking waves have been made by Banner and Fooks (1985), Melville *et al.* (1988), and Trizna *et al.* (1991).

Several attempts have been made to model the backscatter from breaking waves deterministically, based on various assumptions about the geometric structure of the surface. Wetzel (1981, 1990) has constructed models for breaking wave backscatter based on assumptions about the detailed shapes of the scattering elements within an actively breaking region. Lyzenga *et al.* (1983) proposed a wedge diffraction model to account for scattering from the sharp crests of breaking waves, and Kwoh and Lake (1984) made laboratory measurements and calculations to evaluate the relative effects of the sharp crest and the parasitic capillary waves associated with a finite-amplitude surface gravity wave.

Most statistical scattering models of the microwave backscatter from the ocean surface at intermediate incidence angles have been based on Bragg or two-scale approximations (e.g. Valenzuela, 1978). Phillips (1988) has suggested that the radar cross section of the ocean surface may be represented as the sum of separate contributions from Bragg scattering and individual wave breaking events but did not specify the scattering mechanism for these events.

In the following, the Kirchhoff approximation discussed in section 3.1 is combined with the statistical description of a breaking wave surface discussed in section 2.5 in order to construct a model for the backscatter from breaking waves.

Using the Gaussian surface height autocovariance function discussed in section 2.5, the function $\Gamma(x, y)$ which enters the Kirchhoff approximation can be written as

$$\begin{aligned}\Gamma(r) &= \Gamma_b(r) \Gamma_{nb}(r) \\ &= [\Gamma_b(r) - \Gamma_b(\infty)] \Gamma_{nb}(r) + \Gamma_b(\infty) \Gamma_{nb}(r)\end{aligned}$$

where

$$\Gamma_b(r) = \exp \{ 4k_z^2 [\phi_b(r) - \phi_b(0)] \}, \quad \Gamma_b(\infty) = e^{-4k_z^2 h_b^2}$$

and

$$\Gamma_{nb}(r) = \exp \{ 4k_z^2 [\phi_{nb}(r) - \phi_{nb}(0)] \}.$$

If we further assume that the correlation length in the absence of breaking is much longer than r_c , we can approximate this function as

$$\begin{aligned} \Gamma(r) &\approx [\Gamma_b(r) - \Gamma_b(\infty)] \Gamma_{nb}(0) + \Gamma_b(\infty) \Gamma_{nb}(r) \\ &= \Gamma_b(r) - \Gamma_b(\infty) + \Gamma_b(\infty) \Gamma_{nb}(r). \end{aligned}$$

Substituting this into the Kirchhoff approximation, the radar cross section per unit area in the presence of wave breaking becomes

$$\sigma_o = \sigma_b + \sigma_{nb} e^{-4k_z^2 h_b^2}$$

where σ_{nb} is the radar cross section per unit area in the absence of breaking, and

$$\sigma_b = \frac{1}{\pi} k_o^2 \sec^2 \theta \iint [\Gamma_b(r) - \Gamma_b(\infty)] e^{-2ik_b r \cos \phi'} r dr d\phi'.$$

To evaluate this expression, we make another simplifying assumption and approximate the integrand by a second gaussian function, i.e.

$$\Gamma_b(r) - \Gamma_b(\infty) \approx (1 - e^{-4k_z^2 h_b^2}) e^{-r^2/L^2}$$

where L is equal to r_c in the low-frequency limit and approaches the value $r_c / (2k_z h_b)$ in the high-frequency limit. In the intermediate frequency region, the value of L may be approximated by the formula

$$\frac{1}{L^2} = \left(\frac{1}{r_c} \right)^2 + \left(\frac{2k_r h_b}{r_c} \right)^2.$$

The Kirchhoff integral can then be readily evaluated to yield the result

$$\sigma_b = k_o^2 L^2 e^{-k_h^2 L^2} (1 - e^{-4k_r^2 h_b^2}) \sec^2 \theta$$

Before comparing this expression with observations, some of its properties may be noted. First, it can be seen that in the high-frequency limit the radar cross section approaches the value

$$\sigma_b = \left(\frac{r_c}{2h_b} \right)^2 \sec^4 \theta e^{-\left(\frac{r_c}{2h_b} \right)^2 \tan^2 \theta} \quad \text{as } k_o \rightarrow \infty$$

which is recognized as the familiar specular scattering result. Second, in the low-frequency limit or for small grazing angles, the small-argument approximation can be used for the exponential function, and the cross section approaches the limiting value

$$\sigma_b = 4k_o^4 h_b^2 r_c^2 e^{-k_h^2 r_c^2} \quad \text{as } k_o \rightarrow 0 \text{ or } \theta \rightarrow \pi/2.$$

This is equivalent to the result obtained by using the small perturbation method (SPM), except that in this case σ_b is multiplied by $\cos^4 \theta$ for horizontal polarization and $(1 + \sin^4 \theta)$ for vertical polarization. Plots are shown in Figure 11 of the backscatter cross section calculated from the SPM, from a numerical integration of the Kirchhoff integral, and from the analytical approximation to the Kirchhoff integral developed above. Although the Kirchhoff model does not predict the polarization dependence of the backscatter, it does at least provide a transition from the low-frequency to the high-frequency cases and may therefore be expected to be more accurate than the SPM in the intermediate frequency case, although the limits of

Kirchhoff vs. SPM results

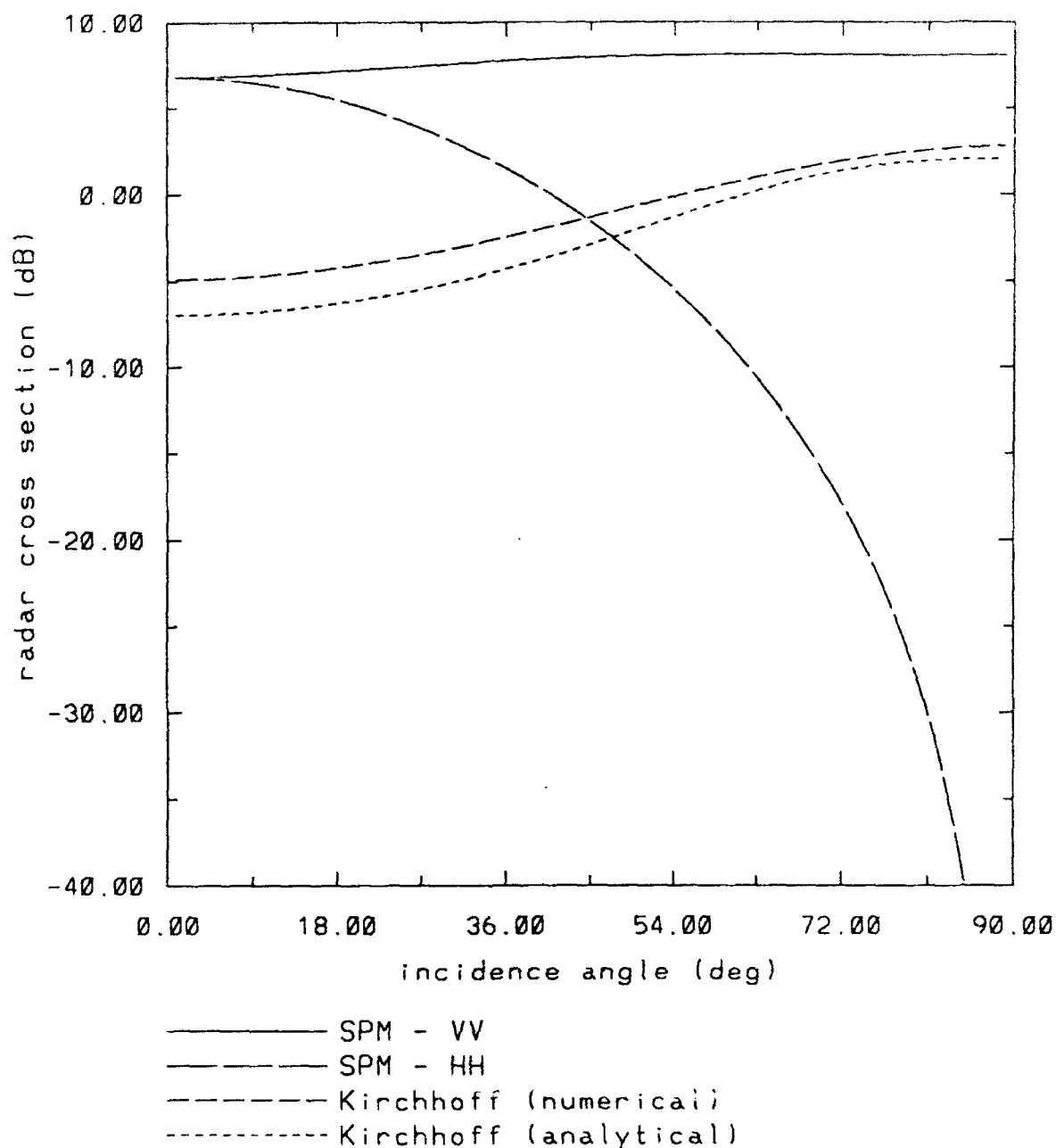


Figure 11. Comparison of X-Band Radar Backscatter Cross Sections Calculated From Kirchhoff and SPM Models for Surface Described by a Gaussian Correlation Function With rms Height and Correlation Length Both Equal to 0.5 cm.

validity of both of these models are still uncertain.

Using the approximate Kirchhoff expression for σ_b derived above, and assuming $r_c = h_b = 0.5$ cm as discussed in section 4, the radar cross section per unit area for $k_o = 2$ rad/cm (X-band) is equal to approximately 1.5 at grazing incidence, which agrees with observations by Lewis and Olin (1980). For the case of large-area averages where a fraction f_b of the surface is covered by breaking water, the contribution of breaking waves to the backscatter can be written as

$$\overline{\sigma_b} = f_b \sigma_b$$

where f_b is the breaking fraction discussed in section 2.5. This expression may be compared with the observations of Jessup *et al.* (1991a, 1991b) by using the breaking fraction f_b as a function of wind speed as shown in Figure 8, and the values of r_c and h_b as estimated in section 2.5. For a radar wavenumber of 2.94 rad/cm (K_u band) and an incidence angle of 45° , the radar cross section per unit area for the breaking areas is approximately 0.66 and the average contribution of these areas to the entire data set is equal to $0.66 f_b$. This contribution is plotted versus the friction velocity (assumed to be 1/30 of the wind speed) and compared with measurements from Jessup *et al.* (1991b) in Figure 12.

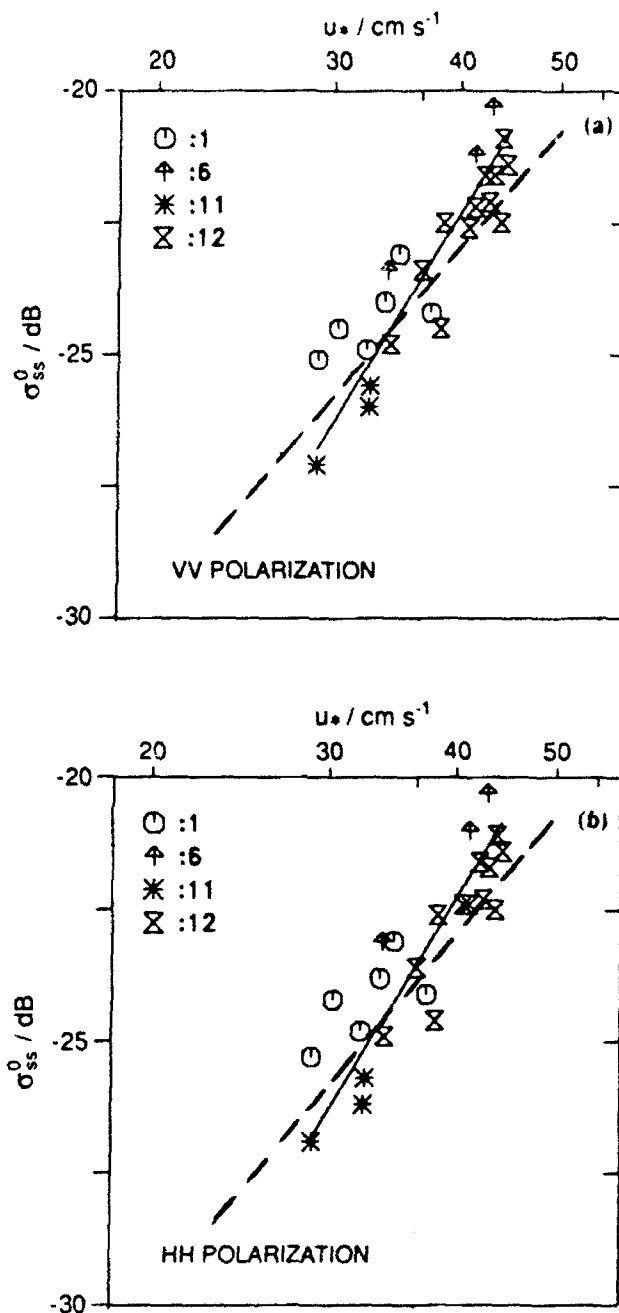


Figure 12. Comparison of Model Predictions (Dashed Line) With Measurements by Jessup *et al* (1991b) of Breaking Wave Contributions to the Average Radar Cross Section of the Ocean Surface.

4.0 MODEL VALIDATION STUDIES

Aside from comparisons with previously published data, model validation activities undertaken during this project centered on the ONR/NRL High Resolution field experiment. This activity involved three areas of participation: (1) experiment planning and pre-experiment model predictions, (2) deployment of a Doppler radar on the Woods Hole LADAS platform, and (3) analysis of SAR and *in situ* data, and comparison with model predictions.

A number of interesting features associated with the edge of the Gulf Stream were observed in both the SAR and RAR images collected during the first High Resolution experiment. These include (1) numerous bright lines, some aligned parallel to the Gulf Stream boundary and some oriented at large angles to this boundary, (2) dark narrow lines parallel to the Gulf Stream currents, and (3) an overall higher return over the Gulf Stream as compared with the shelf water to the west of the stream.

The features in the first category are presumably caused by strong shearing and converging currents. Although these currents were not always clearly observed in the ADCP data because of their shallow depth and rapid spatial variations, some information has been obtained by analyzing a sequence of RAR images (F. Askari, personal communication). An analysis of the radar backscatter variations associated with these features is presented in section 4.2 below.

The second category of features may be due to the accumulation of surfactant materials along weaker convergence or shear regions. Evidence for the association of such features with shearing currents has been observed during previous experiments in which ship wakes crossing similar dark lines were observed to be displaced on either side of the lines (A. Ochadlick, personal communication). However, the connection between the dark lines observed along the edge of the Gulf Stream and any sharp

current gradients in this region has not yet been established.

The higher radar returns observed over the Gulf Stream in some of the radar images may be caused by atmospheric stability effects associated with the higher water temperatures in the Gulf Stream, as discussed in section 2.4 of this report. Further testing of this hypothesis is required using the meteorological data collected during the pilot experiment.

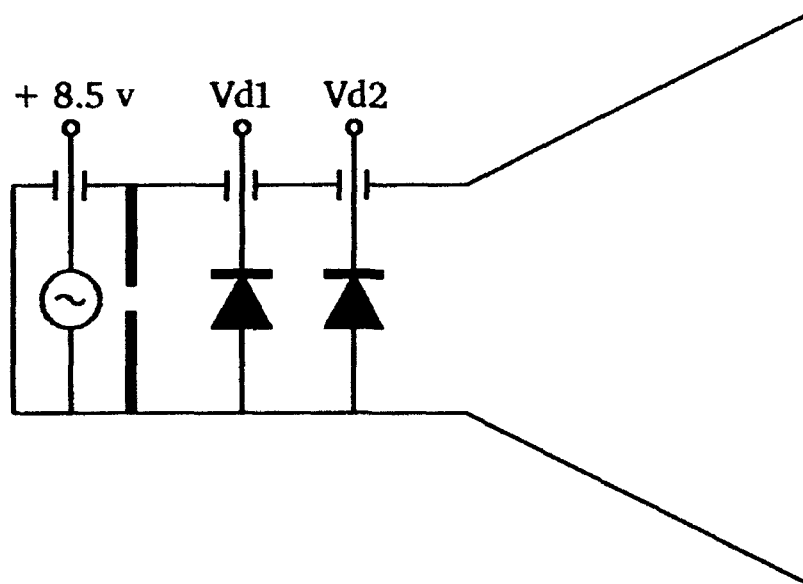
Several of the features observed in the airborne radar images collected during the pilot experiment have been identified in the Doppler radar data set as well. The intention was to compare this data with *in situ* measurements of the surface roughness, surface currents and wind stress in order to test the wave spectrum and radar backscatter models described above. Activities carried out in pursuit of this goal are described in the following section.

4.1. DOPPLER RADAR MEASUREMENTS

During this project, a simple Doppler radar system was assembled using a commercial motion sensing device built by Microwave Associates, and this system was deployed on the Woods Hole LADAS catamaran during the High Resolution field experiment. The MA86735 device consists of a Gunn diode source in a tuned cavity, which is coupled to a short section of waveguide in which two Schottky diode mixers are also mounted (see Figure 13). The other end of the waveguide is connected to a horn antenna which radiates the microwave signal and receives the radiation backscattered by objects or surfaces within its field of view. The electric field at each of the detectors can be represented by

$$E_i = E_{ti} + E_{ri}$$

where E_{ti} is the outgoing or transmitted field and E_{ri} is the incoming or received field at detector i . If this detector is located a distance x_i from the source, the



Frequency = 10.525 GHz

Polarization = Vertical

Antenna Beamwidth = 12 deg.

Figure 13. Schematic Diagram of Doppler Radar. Gunn Diode Source is on the Left. V_{d1} and V_{d2} are the In-Phase and Quadrature Signals From the Detector Diodes.

transmitted field is given by

$$E_{ti} = E_o e^{j(kx_i - \omega t)}$$

and the received field, for a scatterer located at a distance x from the source is

$$E_{ri} = E_o r e^{j(2kx - kx_i - \omega t)}$$

where $k=2\pi/\lambda$ is the radar wavenumber, $\omega=2\pi f$ is the radar frequency in radians/sec and r is the ratio of the transmitted to received field strength (which depends on the radar cross section of the scatterer, its range and position within the antenna beam). Assuming that $r \ll 1$, the voltage on the detector is then given by

$$V_i = |E_{ti} + E_{ri}| = E_o |1 + r e^{j2k(x-x_i)}| \approx E_o [1 + r \cos(2kx - \phi_i)]$$

where $\phi_i = 2kx_i$. Thus, by choosing $\phi_2 - \phi_1 = \pi/2 + n\pi$ or $x_2 - x_1 = (2n+1)\lambda/8$, the in-phase and quadrature components of the signal can be measured. For the MA86735 device, the detector spacing is selected to produce a nominal phase difference of $90^\circ \pm 15^\circ$. Examination of the output signals revealed that the actual detector phasing was about 80° for the particular unit used during the High Resolution experiment. A phase error was also incurred due to the fact that the two detector signals were not sampled exactly simultaneously. These phase errors were corrected and the amplitudes of the two detector signals were equalized during processing of the data.

The detector output signals were fed into two parallel operational amplifiers in order to remove the d.c. bias and amplify the fluctuating part of the signal by a factor of 100 (20 dB). The antenna used was a standard gain horn antenna manufactured by Scientific Atlanta, which has a beamwidth of approximately 12° and a gain of 22.5 dB at the operating frequency of 10.525 GHz. The unit was mounted so as to produce a vertically polarized field with an incidence angle of about 45° . The data was sampled

at a rate of 167 sample pairs per second, using a data acquisition system supplied by the Woods Hole Oceanographic Institution, and recorded on the hard disk of a personal computer.

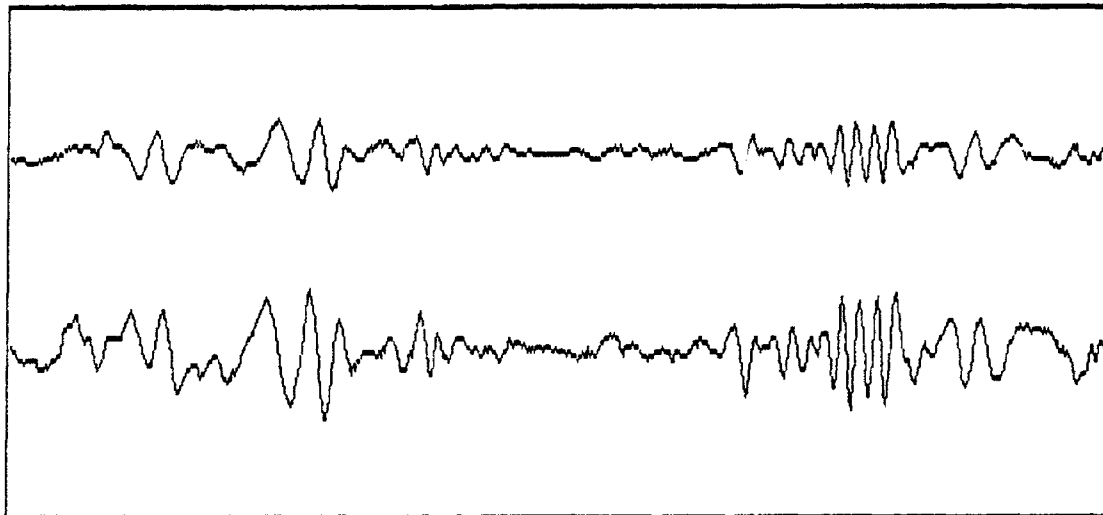
The Doppler radar was mounted on the LADAS catamaran, along with a video camera, laser wave slope gauge and a mini-SODAR for meteorological observations (E. Bock, personal communication). The Doppler radar was mounted next to the video camera on a mast approximately 4 meters above the water surface, as shown in Figure 14. This produced a footprint on the surface having a diameter of about 1 meter.

A total of 18 hours of data was collected during the period 13-24 September, 1991. Examples of the data are shown in Figures 15 and 16. Figure 15 shows the raw I&Q signals recorded during a 3.6 second time interval under low wind conditions on September 16. The data was processed using a short-time Fourier transform method to produce two-dimensional (frequency versus time) plots, as shown in Figure 16. These plots indicate that under these low wind conditions the signal is dominated by an extremely coherent, though time varying, component. Further analysis indicates that this component is probably due to a sidelobe of the antenna gain pattern. The third sidelobe of the horn antenna occurs at an angle of about 44° from the boresight direction, and was therefore directed nearly toward the nadir for the configuration in which the radar was deployed. The theoretical two-way antenna gain for this sidelobe is more than 40 dB below the main lobe. Data from the NRL 4-frequency radar (Valenzuela, 1978) indicates that the radar cross section is typically 25 dB larger at nadir than at 45° incidence, for vertical polarization. However, under low winds it appears that this difference can be much larger and the return from the nadir-looking sidelobe can dominate the main lobe return. In future, it is recommended that a shield be installed below the antenna to eliminate this sidelobe return.



Figure 14. Photograph of Doppler Radar Mounted on the LADAS Platform. Radar is on the Near Side of the Mast, Next to Video Camera.

Mon Sep 16 12:49:29 1991



Blocks 217 to 222
Hit C to continue or S to stop

**Figure 15. Examples of Doppler Radar In-Phase and Quadrature Signals
Recorded During the High Resolution Field Experiment.**

16 SEPTEMBER 1991
12:51:29 - 12:52:29 EST



time →

vertical dimension is Doppler frequency
from -83 to +83 Hz (-1.25 m/s to + 1.25 m/s)

aperture = 32 samples (0.19 sec)

Figure 16. Plot of Doppler Spectrum Versus Time, Obtained From Radar Signals
Recorded on September 16, 1991.

This problem did not appear to be present, at least to the same degree, on September 17 during a crossing of the 'rip' feature which was the focus of much attention during the first High Resolution experiment. A plot of the backscattered power (in relative units) from the Doppler radar during one of these crossings is shown in Figure 17. The average backscattered power during the interval from 16:17:15 to 16:19:15 EDT was five times greater than the average power during the interval from 16:16:30 to 16:16:45. This increase is somewhat smaller than the maximum change observed by the NRL airborne real-aperture radar (F. Askari, personal communication) for the same or a similar feature. The difference may be due to a difference in the radar look direction, or may reflect some contamination of the Doppler radar signal by the sidelobe return in the low-return area just prior to the rip crossing.

Because of problems with the WHOI laser slope gauge, as well as the aforementioned problems with the Doppler radar, the original intention of using the combination of these data sets for model verification purposes has been largely unfulfilled. Instead, a collaborative effort with Peter Smith of NRL/Stennis has been initiated, utilizing his measurements of the wave spectrum from a buoy as it drifted across the rip feature, and a comparison of model predictions with SAR observations has also been carried out as described in the following section.

4.2. SAR DATA ANALYSIS

Data was collected with the P3 SAR system on six days during the first High Resolution field experiment, on September 11, 12, 16, 19, 20 and 21. Of these data sets, the ones collected on the 16th appear to contain the largest number of interesting features in the vicinity of the research vessels, and these have consequently received the most attention. In fact, the only digitally processed data available during the period of this project was from data set 1 (pass 2) on the 16th. Our analysis has

17 SEPTEMBER 1991

16:16:25 - 16:20:25 EST

RECEIVED POWER

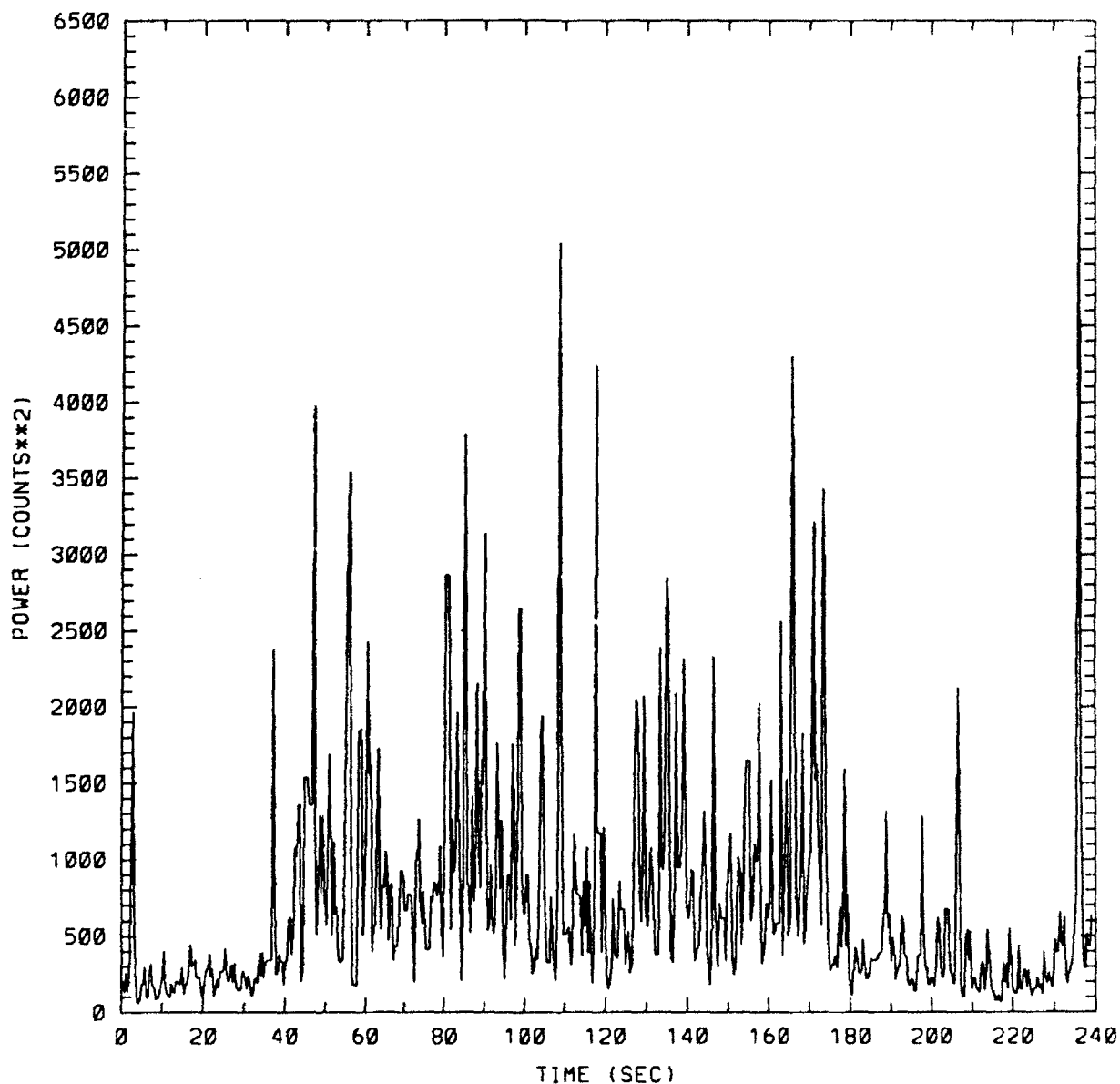


Figure 17. Backscattered Power Received by Doppler Radar on September 17, 1991 During a Crossing of the 'Rip' Feature.

therefore concentrated on this data set.

On the morning of September 16, the USNS Bartlett executed a box pattern centered at approximately 35° 16'N and 75° 5'W. The box was oriented at about 45° from North so that the northeast and southwest edges of the box intersected the edge of the Gulf Stream at approximately right angles. Two distinct changes in the water temperature were observed aboard the Bartlett at 10:45 and 10:54 EDT while heading southeast into the Gulf Stream, on the first leg of the box pattern. The chief scientist's log indicates the following entry at 10:54: "Crossing scum line.

Athwartship speed jumped from below 1 knot (where it has been all this time) to 1.8 then 2.2 knots. Perturbation in gyro heading was about 4 deg, indicating a current front so sharp the auto heading device couldn't respond fast enough. STAR saw stratified water before scum line, changing to isothermal water after it " (G. Marmorino, personal communication).

SAR data set 1 (pass 2) was collected over this area at approximately 12:08 EDT. A segment of this pass was digitally processed by NAWC, covering the area shown in Figure 18. In order to compensate for the time difference between the overpass and the ship observations, the locations of the water parcels sampled by the ship at 10:45 and 10:54 EDT were projected using the water velocities measured by the Bartlett's ADCP, i.e. 50.8 cm/s toward 31.4 °T at 10:45 and 67.6 cm/s toward 42.9 °T at 10:54. These projected locations are also shown in Figure 18, along with the outline of a subset of the digitally processed image which was selected to include these points. The Lvv and Xvv band SAR images for this subset are shown in Figure 19. Based on the position information, which is of course somewhat uncertain because of the relatively large time difference between the shipboard and aircraft observations, we conclude that the two bright lines running diagonally through the image subset shown in Figure 19 correspond to the two thermal gradients observed aboard the Bartlett, with the rightmost line corresponding to the scum line and

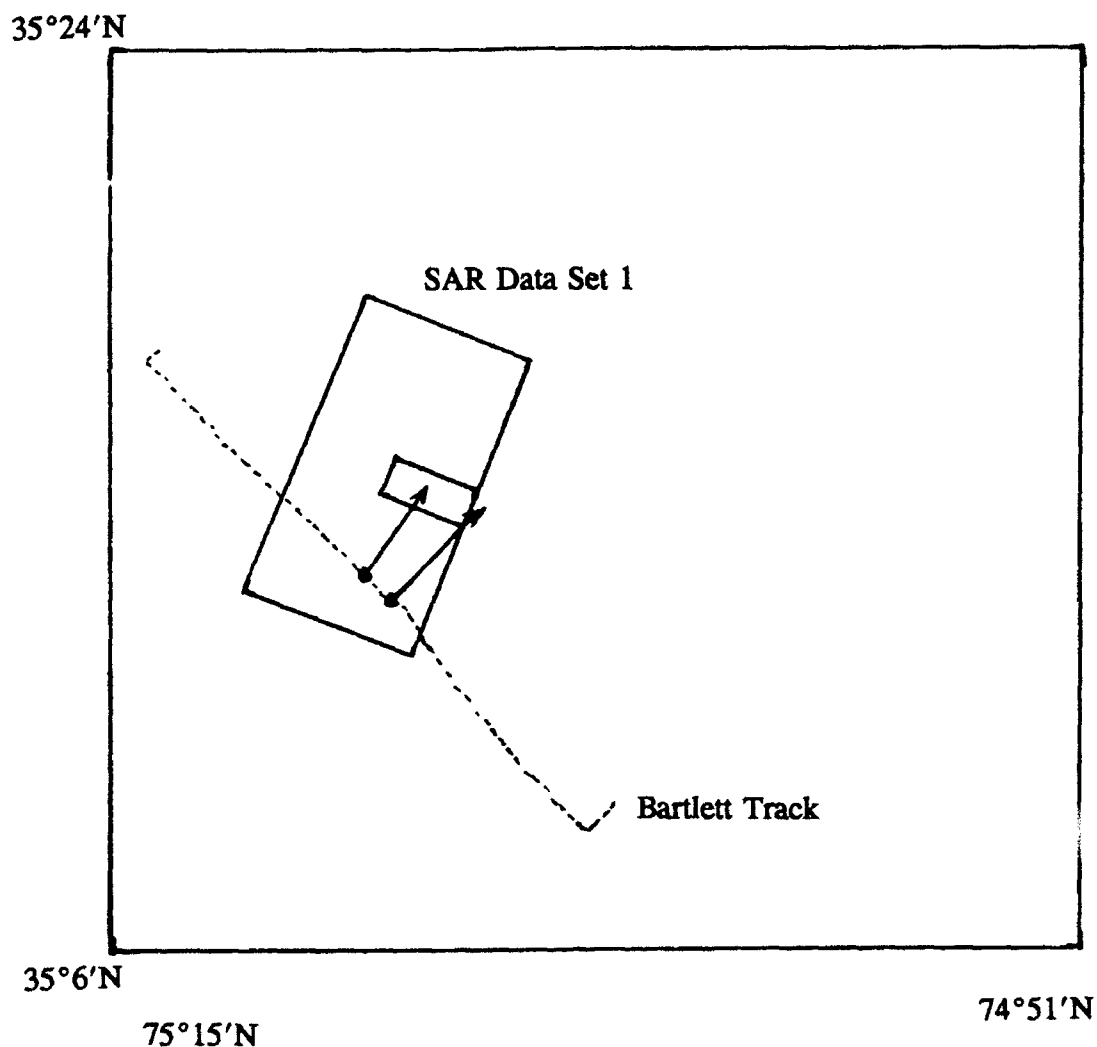
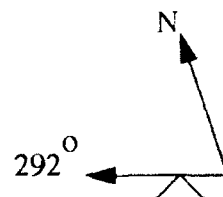
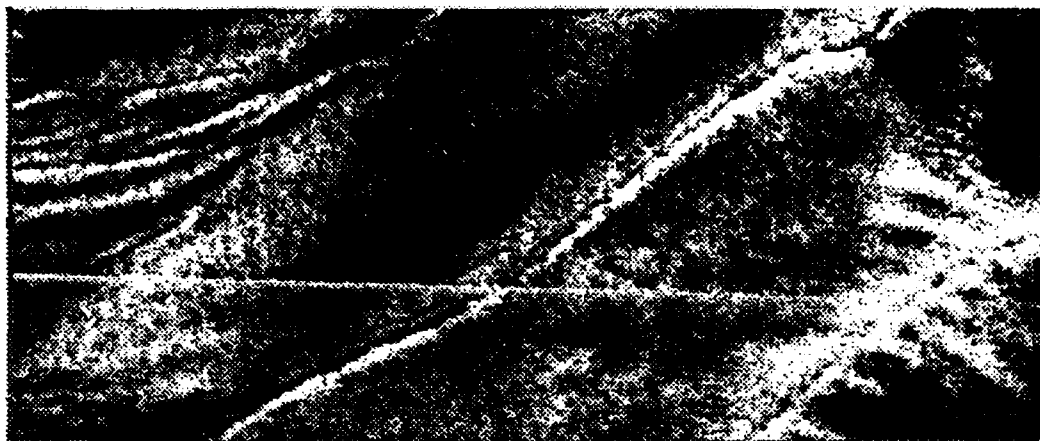


Figure 18. Location of P3 SAR Data Set 1 (Pass 2) Relative to Bartlett Track From 10:00 to 12:00 EDT on September 16, 1991. Dots Indicate Locations of Sharp Thermal Gradients, and Arrows Represent Projected Locations of These Points at the Time of the SAR Overpass (12:08 EDT). Smaller Box Indicates Location of Image Subset Shown in Figure 19.

SAR Data Set 1 9/16/91



L vv



X vv

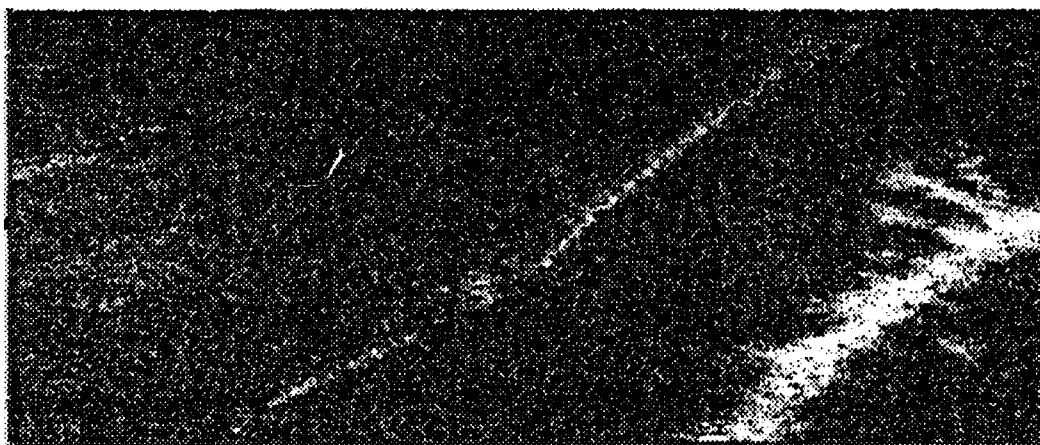


Figure 19. L-Band and X-Band Images for Subset Indicated in Figure 18. Horizontal Line Through L-Band Image is the "Double-Nadir" Return Which Occurs at an Incidence Angle of 60°. Image Dimensions are 170 x 410 Pixels or 1377 x 3321 Meters, Each Pixel Representing the Sum of 3 x 5 Original One-Look Pixels.

velocity gradient noted in the chief scientist's log.

It is interesting to note that the orientation of these features (approximately 70°T) is much different from the measured current direction, which suggests the possibility of a strong converging as well as shearing current. The current variations in the vicinity of these features which were noted in the chief scientist's log were not clearly observed by the ADCP, apparently because the horizontal and/or vertical resolution of the measurements was insufficient to resolve the features. However, an apparently similar feature (dubbed the 'rip' feature) was observed 25 hours later by both the ships and the NRL airborne real-aperture radar at around $35^\circ 23'\text{N}$ and $75^\circ 0'\text{W}$, i.e. about 18 km north of the features in the SAR image. These features appear to correspond with 'shingles' protruding from the North edge of the Gulf Stream, which are visible on AVHRR thermal images and are observed on these images to migrate Northward about 20 km per day. The convergence velocities in these features have been estimated from various sources (including a sequence of NRL RAR images) to be on the order of 25-40 cm/s.

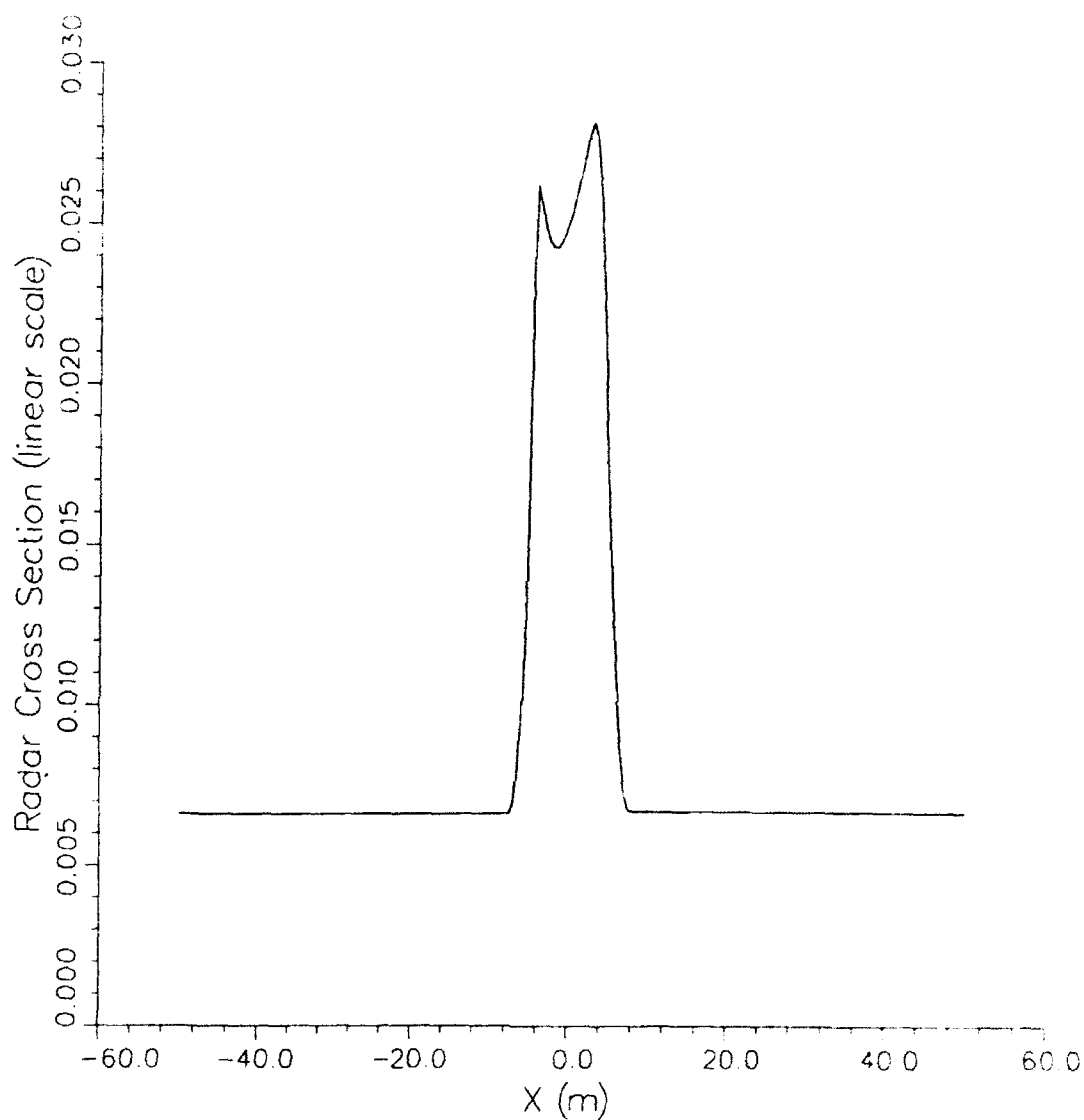
The nearest available wind measurement was made aboard the R/V Oceanus at 11:30 EDT on September 16, when the Oceanus was located at $35^\circ 16'\text{N}$ and $75^\circ 0'\text{W}$. This measurement indicated a wind speed of 4.2 m/s from 161°T (J. Edson, personal communication). In attempt to match the spectral shapes measured by Jähne and Riemer (1990) more closely at low wind speeds, the net source function discussed in section 2.1 was modified by increasing the dissipation rate for wavenumbers larger than 1 rad/cm. The angular distribution of the growth rate was also modified so as to produce the ratio of upwind to downwind propagating waves inferred by Plant and Keller (1990) from L-band Doppler radar measurements. The current field was approximated by a linear variation in both the normal and tangential components of the current from -20 cm/s to +20 cm/s over a 10 meter transition region.

Changes in the wave spectrum due to the interaction of the ambient wave field

with this current were calculated using the model described in Lyzenga (1991). Changes in the radar backscatter at L-band and X-band were then calculated using the two-scale model described by Plant (1986). These results are shown as the solid lines in Figures 20 and 21. The contribution to the backscatter from breaking waves was also calculated using the model described in sections 2.5 and 3.3 of this report. This contribution is indicated by the dashed line in Figure 21. The slope variance used for this calculation, as obtained from the wave-current interaction model, is shown in Figure 22.

The change in backscatter from the two-scale model (without wave breaking effects) is much smaller at X-band than at L-band, as discussed in Lyzenga (1991). When breaking effects are included, the changes in backscatter at X-band and L-band are comparable, for this case, both being on the order of 7-8 dB. This appears to agree qualitatively with the SAR images shown in Figure 19. A quantitative comparison is difficult because the background signal, at least for the X-band image, appears to be below the noise floor. Plots of the image intensity across the feature (taken from the right-hand side of Figure 19) are shown in Figures 23 and 24. From these plots, the ratio of the peak to background signal can be inferred to be at least a factor of 6 (7.8 dB) at X-band and a factor of 12 (10.8 dB) at L-band. It may also be noted that some weaker features can be seen in the L-band image which do not appear to be present in the X-band image. This is explainable in the context of the present theory by reference to the fact that the breaking wave return is a strongly nonlinear function of the slope variance.

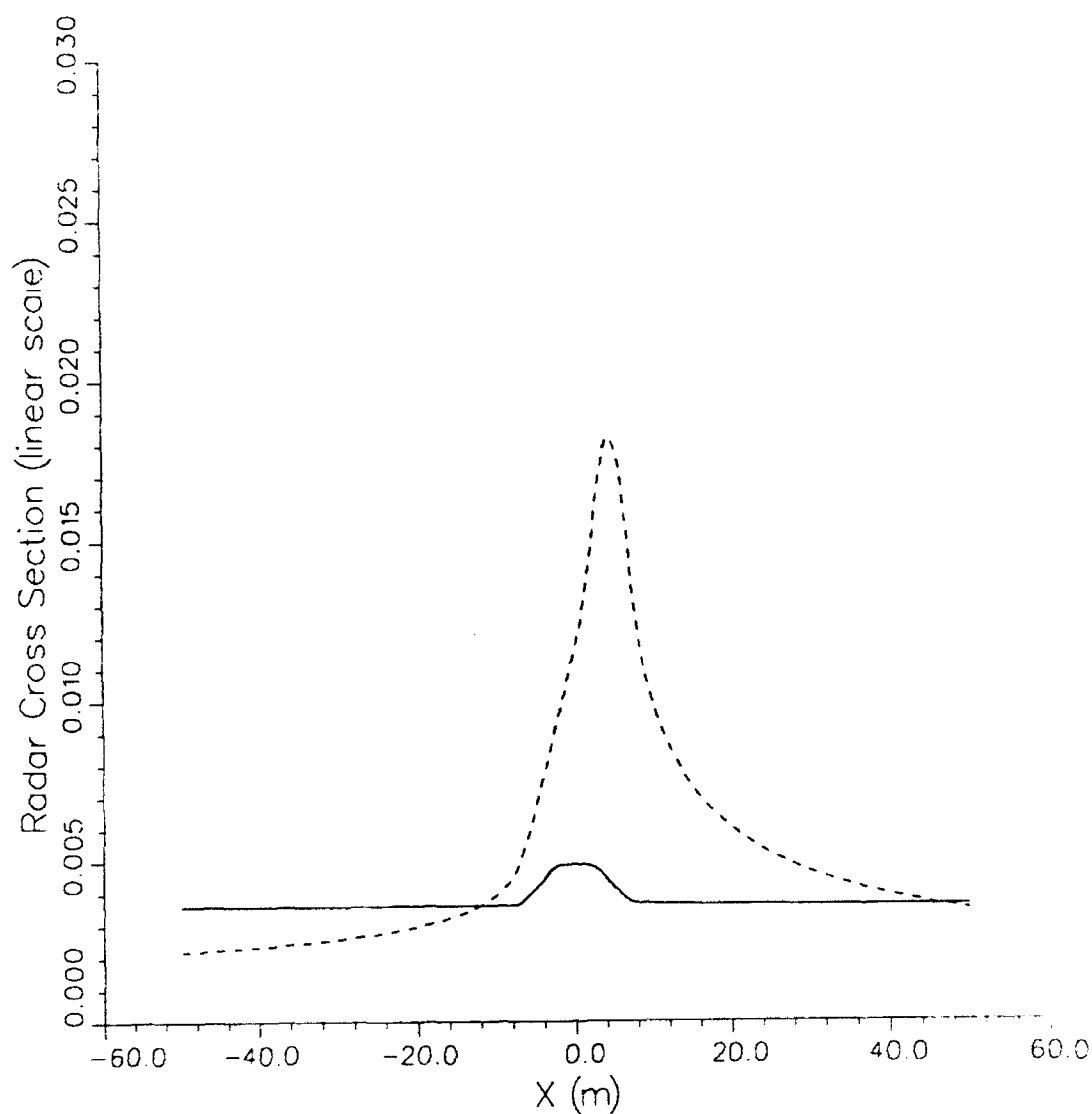
25.0 cm, V-pol, 60 deg inc, 45 deg az



LEGEND
Two-Scale RCS

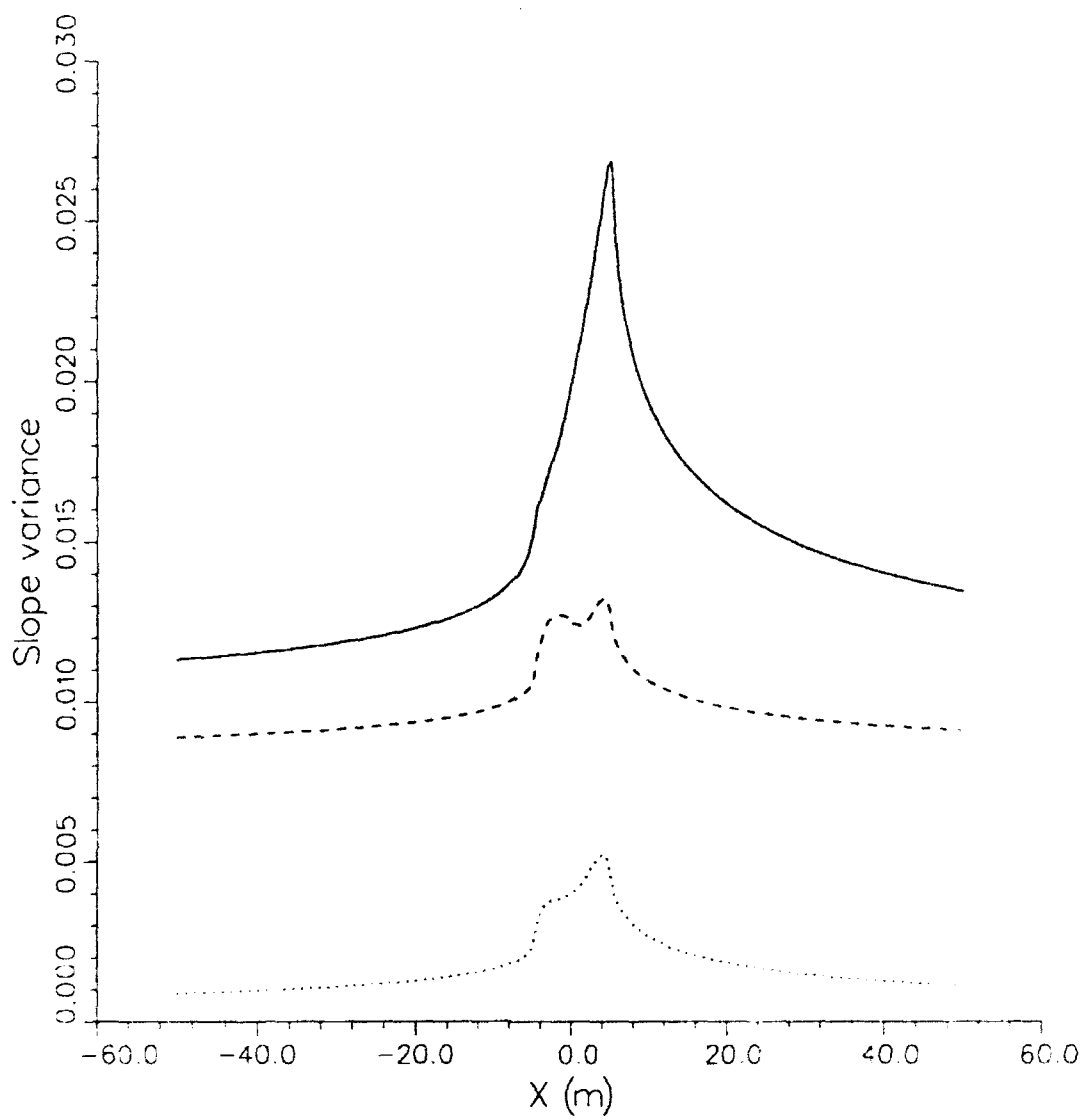
Figure 20. L-Band Radar Cross Section Variations Across 'Rip' Current Feature, Calculated From Wave-Current Interaction Model Combined With Two-Scale Radar Backscatter Model.

3.0 cm, V-pol, 60 deg inc, 45 deg cz



LEGEND
Two-Scale RCS
 --- Wave Breaking RCS ---

Figure 21. X-Band Radar Cross Section Variations Across 'Rip' Current Feature, Calculated From Two-Scale Model (Solid Line) and Breaking Wave Model (Dashed Line).



LEGEND
 x-component
 y-component
 x-y covariance

Figure 22. Slope Variances Calculated From Wave-Current Interaction Model for 'Rip' Feature.

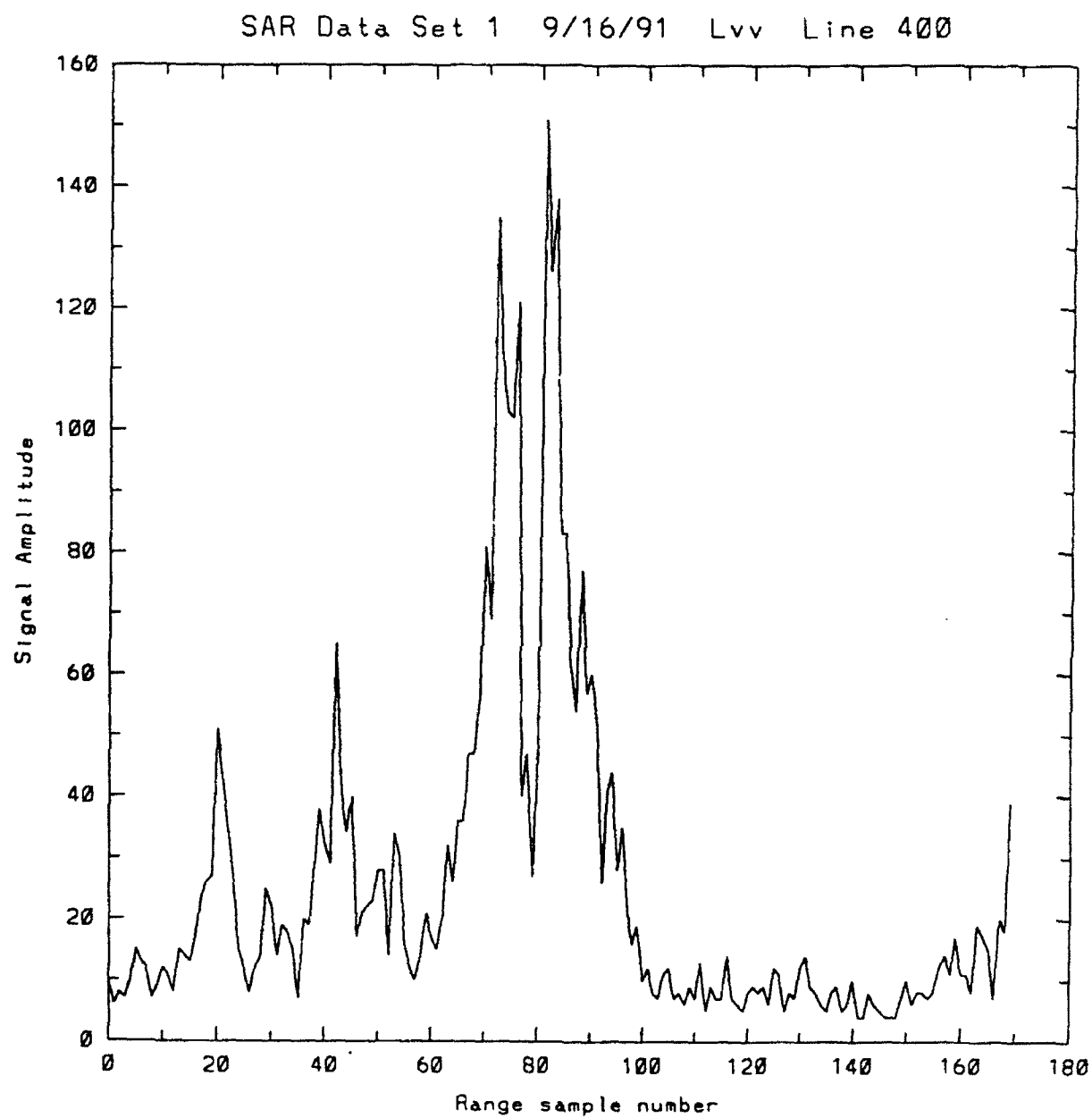


Figure 23. L-Band Image Signals Taken From a Vertical Cut Through the Right-Hand Side of Image Shown in Figure 19.

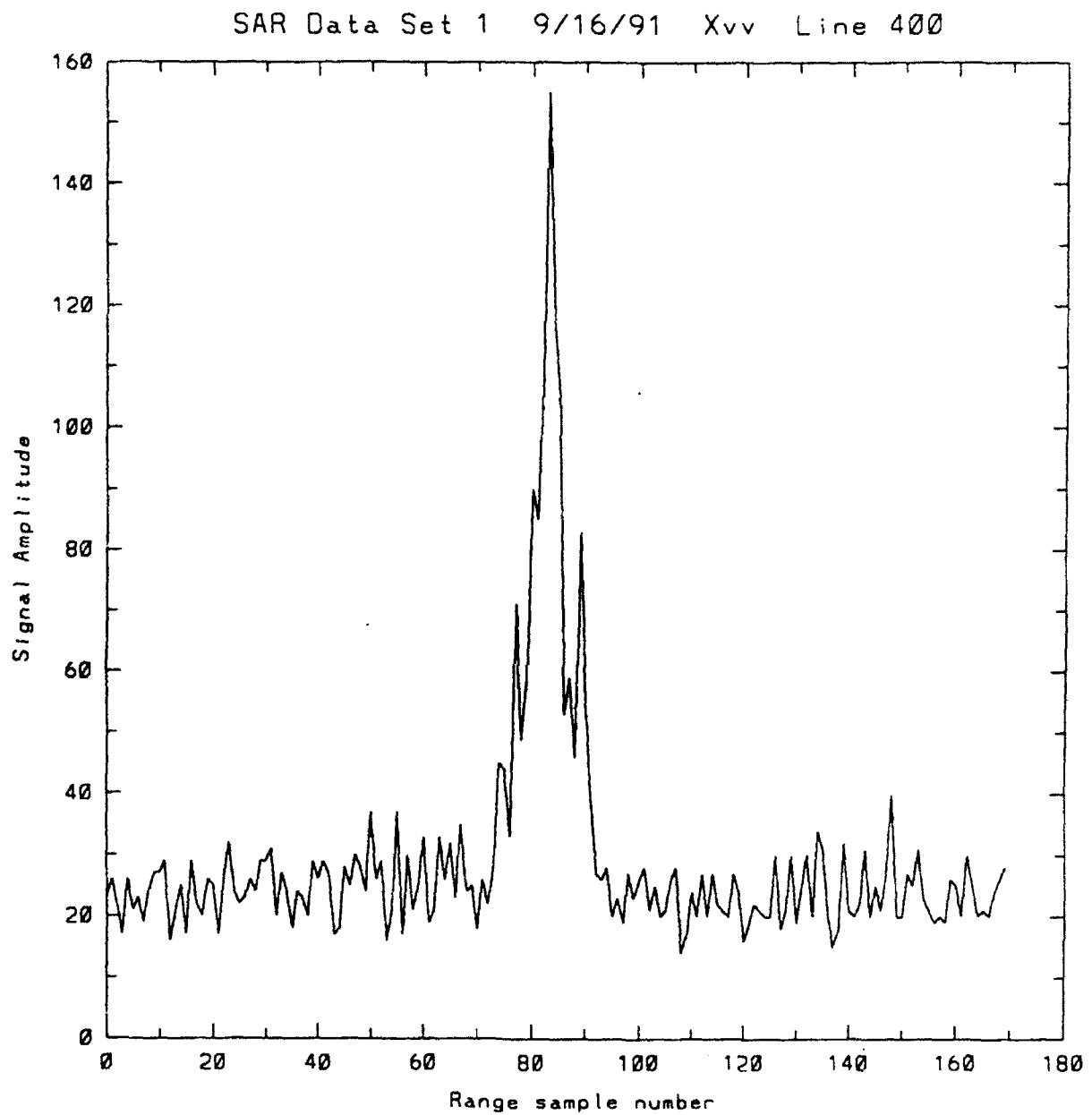


Figure 24. X-Band Image Signals Taken From a Vertical Cut Through the Right-Hand Side of Image Shown in Figure 19.

5.0 SUMMARY AND CONCLUSIONS

During this project, a new analytic solution of the wave action equation was derived, and various formulations were investigated for the net source function which appears in this equation. The present formulation includes source terms due to the Phillips growth mechanism and the Miles or exponential growth mechanism, and dissipation terms due to viscosity, surfactant damping, and wave breaking. Coefficients have been selected so as to yield an equilibrium spectrum which is in reasonable agreement with observations. However, considerable uncertainty exists with respect to several of these terms and the present formulation can only be considered as provisional.

One area in which the present formulation of the net source function is quite clearly lacking is in its neglect of nonlinear interactions, which involve the transfer of energy from one region of the spectrum to another. As a first step in this direction, a model for the effects of wave breaking was developed, which describes the contribution of breaking waves in terms of the breaking fraction, which is a function of the slope variance. This model appears to predict the wind speed dependence of the surface curvature spectrum at wavenumbers between 1 and 8 rad/cm. The electromagnetic scattering from breaking waves is calculated using the Kirchhoff approximation, and the results are found to compare favorably with several observations of the radar backscatter from breaking waves.

The combined model predicts that the radar backscatter at centimeter wavelengths is strongly and nonlinearly dependent on the slope variance associated with wavenumbers below about 1 rad/cm. In the open ocean, this variance is linearly related to the wind speed or friction velocity. However, in the presence of variable surface currents, the slope variance may also change dramatically due to the interaction of surface waves with these currents. Comparison of the predictions of

this model with SAR observations during the first High Resolution field experiment appear favorable, but of course many more such comparisons are required in order to adequately test the model.

6.0 REFERENCES

- Banner, M.L. and E.H. Fooks, On the microwave reflectivity of small-scale breaking water waves, *Pro. R. Soc. London, Ser. A*, 399, 93-109, 1985.
- Barrick, D.E., Rough surface scattering based on the specular point theory, *IEEE Trans. Antennas Propag.*, AP-16, 449-454, 1968.
- Bjerkaas, A.W. and F.W. Riedel, Proposed model for the elevation spectrum of a wind-roughened sea surface, *JHU/APL Tech. Memo. No. TG-1328*, 31 pp., Johns Hopkins University, Laurel, MD, 1979.
- Cini, R. and P.P. Lombardini, Experimental evidence of a maximum in the frequency domain of the ratio of ripple attenuation in monolayered water to that in pure water, *J. Colloid Interface Sci.* 81, 125-131, 1981.
- Cini, R., P.P. Lombardini, C. Manfredi, and E. Cini, Ripples damping due to monomolecular films, *J. Colloid Interface Sci.* 119, 74-80, 1987.
- Cox, C. and W. Munk, Statistics of the sea surface derived from sun glitter, *J. Mar. Res.*, 13, 198-227, 1954.
- Dorrestein, R., General linearized theory of the effect of surface films on water ripples, *Proc. Amsterdam Academy of Sci.* B54, 260-272, 1951.
- Holliday, D., G. St-Cyr, and N.E. Woods, A radar ocean imaging model for small to moderate incidence angles, *Int. J. Remote Sens.*, 7, 1809-1834, 1986.
- Holliday, D., Resolution of a controversy surrounding the Kirchhoff approach and the small perturbation method in rough surface scattering theory, *IEEE Trans. Antennas Propag.*, 35, 120-122, 1987.
- Jähne, B. and K.S. Riemer, Two-dimensional wave number spectra of small-scale water surface waves, *J. Geophys. Res.*, 95, 11531-11546, 1990.
- Jessup, A.T., W.C. Keller, and W.K. Melville, Measurements of sea spikes in microwave backscatter at moderate incidence, *J. Geophys. Res.*, 95, 9679-9688, 1990.

REFERENCES (CONTINUED)

Jessup, A.T., W.K. Melville, and W.C. Keller, Breaking waves affecting microwave backscatter, 1. Detection and Verification, *J. Geophys. Res.*, **96**, 20547-20559, 1991a.

Jessup, A.T., W.K. Melville, and W.C. Keller, Breaking waves affecting microwave backscatter, 2. Dependence on wind and wave conditions, *J. Geophys. Res.*, **96**, 20561-20569, 1991b.

Kondo, J., Y. Fujinawa, and G. Naito, High-frequency components of ocean waves and their relation to the aerodynamic roughness, *J. Phys. Oceanog.*, **3**, 197-202, 1973.

Kwoh, D.S. and B.M. Lake, A deterministic, coherent, and dual-polarized laboratory study of microwave backscattering from water waves, 1, Short gravity waves without wind, *IEEE J. Oceanic Eng.*, **OE-9**, 291-308, 1984.

Levich, V.G., *Physicochemical Hydrodynamics*, Chapter 11, Prentice-Hall. Englewood Cliffs, New Jersey, 1962.

Lewis, B.L. and I.D. Olin, Experimental study and theoretical model of high-resolution radar backscatter from the sea, *Radio Sci.* **15**, 815-828, 1980.

Longuet-Higgins, M.S., On wave breaking and the equilibrium spectrum of wind-generated waves, *Proc. R. Soc. London, Ser. A*, **310**, 151-159, 1969.

Lyzenga, D.R., A.L. Maffett, and R.A. Shuchman, The contribution of wedge scattering to the radar cross section of the ocean surface, *IEEE Trans. Geosci. Remote Sens.*, **GE-21**, 502-505, 1983.

Lyzenga, D.R. and J.R. Bennett, Full-spectrum modeling of synthetic aperture radar internal wave signatures, *J. Geophys. Res.* **93**, 12345-12354, 1988.

Lyzenga, D.R., Interaction of short surface and electromagnetic waves with ocean fronts, *J. Geophys. Res.* **96**, 10765-10772, 1991.

Melville, W.K., M.R. Loewen, F.C. Felizardo, A.T. Jessup, and M.J. Buckingham, Acoustic and microwave signatures of breaking waves, *Nature*, **336**, 54-59, 1988.

REFERENCES (CONTINUED)

- Ochi, M.K. and C-H. Tsai, Prediction of occurrence of breaking waves in deep water, *J. Phys. Oceanogr.*, 13, 2008-2019, 1983.
- Pierson, W.J. and L. Moskowitz, A proposed spectral form for fully developed seas based on the similarity theory of S.A. Kitaigorodskii, *J. Geophys. Res.*, 69, 5181-5190, 1964.
- Pierson, W.J. and R.A. Stacy, The elevation, slope, and curvature spectra of a wind roughened sea surface, *NASA Contract Rep. No. CR-2247*, 129 pp., 1973.
- Phillips, O.M., On the generation of waves by turbulent wind, *J. Fluid Mech.*, 2, 417-495, 1957.
- Phillips, O.M., *The Dynamics of the Upper Ocean*, 2nd. ed., 336pp., Cambridge University Press, New York, 1977.
- Phillips, O.M., Spectral and statistical properties of the equilibrium range in wind-generated gravity waves, *J. Fluid Mech.*, 156, 505-531, 1985.
- Phillips, O.M., Radar returns from the sea surface - Bragg scattering and breaking waves, *J. Phys. Oceanogr.*, 18, 1065-1074, 1988.
- Plant, W.J., A relationship between wind stress and wave slope, *J. Geophys. Res.*, 87, 1961-1967, 1982.
- Plant, W.J., A two-scale model of short wind-generated waves and scatterometry, *J. Geophys. Res.* 91, 10735-10749, 1986.
- Plant, W.J. and W.C. Keller, Evidence of Bragg scattering in microwave Doppler spectra of sea return, *J. Geophys. Res.*, 95, 16299-16310, 1990.
- Snyder, R.L., F.W. Dobson, J.A. Elliott, and R.B. Long, Array measurements of atmospheric pressure fluctuations above surface gravity waves, *J. Fluid Mech.*, 102, 1-59, 1981.
- Snyder, R.L. and R.M. Kennedy, On the formation of whitecaps by a threshold mechanism. Part I: Basic Formalism. *J. Phys. Oceanogr.*, 13, 1482-1492, 1983.

REFERENCES (CONCLUDED)

Spillane, M.C., E.C. Monahan, P.A. Bowyer, D.M. Doyle, and P.J. Staben, Whitecaps and global fluxes, pp. 209-218 in *Oceanic Whitecaps*, E.C. Monahan and G. Mac Niocaill, eds., Reidel Pub. Co., Dordrecht, 1986.

Srokosz, M.A., On the probability of wave breaking in deep water. *J. Phys. Oceanogr.*, *16*, 382-385, 1986.

Thompson, D.R., Calculation of radar backscatter modulations from internal waves, *J. Geophys. Res.*, *93*, 12371-12380, 1988.

Trizna, D.B., J.P. Hansen, P. Hwang, and J. Wu, Laboratory studies of radar sea spikes at low grazing angles, *J. Geophys. Res.*, *96*, 12529-12537, 1991.

Valenzuela, G.R., Theories for the interaction of electromagnetic and oceanic waves - a review, *Boundary-Layer Met.*, *13*, 61-85, 1978.

Wetzel, L.B., On microwave scattering by breaking waves, in *Wave Dynamics and Radio Probing of the Ocean Surface*, ed. by O.M. Phillips and K. Hasselmann, pp. 273-284, Plenum, New York, 1986.

Wetzel, L.B., Electromagnetic scattering from the sea at low grazing angles, in *Surfaces Waves and Fluxes, Vol. II - Remote Sensing*, ed. by G.L. Geernaert and W.J. Plant, pp. 109-171, 1990.

APPENDIX

Interaction of Short Surface and Electromagnetic Waves With Ocean Fronts

DAVID R. LYZENGA

Advanced Concepts Division, Environmental Research Institute of Michigan, Ann Arbor

The interaction of short surface waves with shearing and converging currents is investigated by means of an approximate analytical solution of the wave action spectral transport equation. Spectral perturbations of less than 10% are predicted at centimeter wavelengths for moderately strong ocean fronts, although much larger perturbations are expected at wavelengths of the order of 1 m. These results, when combined with a simple Bragg electromagnetic scattering model, do not explain the large backscatter variations observed at X band and C band in the vicinity of ocean fronts. A two-scale electromagnetic scattering model provides an effective coupling between the long-wave spectral perturbations and the radar backscatter at small incidence angles, but this mechanism becomes less effective at intermediate incidence angles. Observation of large backscatter variations at these angles may thus be an indication of additional hydrodynamic and/or electromagnetic scattering mechanisms that are not yet accounted for.

1. INTRODUCTION

Ocean fronts are characterized by large horizontal and vertical gradients in the fluid velocity as well as density (i.e., temperature and/or salinity). Surface water flows toward the front and is subducted at the frontal boundary, causing a converging current at the surface. The component of the current parallel to the front is also frequently observed to have an intense horizontal shear, particularly in the case of larger-scale ocean fronts [Garvine and Monk, 1974]. These two types of surface current variations are illustrated in Figure 1. The interaction of surface waves with these currents causes a change in the surface roughness, which also implies a change in the radar reflectivity of the surface. As a result, linear features can frequently be observed in radar images of the ocean where fronts are known to occur [e.g., Larson *et al.*, 1976; Mattie *et al.*, 1980; Hayes, 1981; Vesecky and Stewart, 1982; Fu and Holt, 1983]. Other mechanisms may also be involved in some cases, including variations in wind stress associated with temperature changes across the front and damping of short surface waves by surfactant materials accumulated along the front.

In this paper the wave-current interaction mechanism is explored as a possible explanation for the appearance of fronts in radar images of the ocean surface. An approximate solution of the wave action spectral transport equation is derived in the following section. The properties of this solution are described in section 3, and the implications for radar imaging of ocean fronts are discussed in section 4.

2. WAVE-CURRENT INTERACTIONS

The interaction of surface waves with a steady, one-dimensional current field (i.e., a current which is a function of only one spatial variable) can be described in terms of the action spectral transport equation

$$(c_{gx} + u) \frac{\partial N}{\partial x} - \left(k_x \frac{du}{dx} + k_y \frac{dv}{dx} \right) \frac{\partial N}{\partial k_x} = f_S(N) \quad (1)$$

where c_{gx} is the x component of the wave group velocity; u and v are the x and y components of the surface current, respectively; k_x and k_y are the x and y components of the wave number; N is the action spectral density, which is defined as the energy spectral density divided by the wave frequency; and $f_S(N)$ represents the net source function for wave action, which implicitly includes the effects of air-sea interactions, nonlinear wave-wave interactions, viscous dissipation, and other dissipation mechanisms such as wave breaking [Phillips, 1984].

The form of the net source term on the right-hand side of (1) is quite uncertain. In fact, it is not clear that it can safely be assumed to be only a local function of N since energy may be exchanged among different regions of the spectrum by nonlinear interactions. However, this assumption has been provisionally adopted for the sake of simplicity, until the importance of these nonlocal effects is demonstrated and a satisfactory method of accounting for them is devised. The existence of a stable equilibrium condition in the absence of any currents implies that $f_S(N_0) = 0$ and $f'_S(N_0) < 0$ where N_0 is the equilibrium spectral density. Expanding $f_S(N)$ in a Taylor series about this point, we can then write

$$f_S(N) = -\beta_r(N - N_0) + \gamma(N - N_0)^2 + \dots \quad (2)$$

where $\beta_r = -f'_S(N_0)$ and $\gamma = \frac{1}{2}f''_S(N_0)$. If higher-order terms are neglected, and if the condition $f_S(0) = 0$ is imposed, this form is equivalent to that used by Hughes [1978], with $\beta_r = -N_0\gamma = \beta$ where β is the initial growth rate due to wind input. If higher-order terms are included, the relaxation rate β_r is not necessarily equivalent to the growth rate β .

Using this expansion for the right-hand side, it is convenient to rewrite the spectral transport equation as

$$(c_{gx} + u) \frac{\partial f}{\partial x} + \beta_r f = \mu(x, k_x, k_y) + \epsilon, \quad (3)$$

where $f = N/N_0 - 1$ is the fractional spectral perturbation or deviation from the equilibrium state,

$$\mu(x, k_x, k_y) = \left(k_x \frac{du}{dx} + k_y \frac{dv}{dx} \right) \frac{1}{N_0} \frac{\partial N_0}{\partial k_x} \quad (4)$$

Copyright 1991 by the American Geophysical Union.

Paper number 91JC00900.
0148-0227/91/91JC-00900\$05.00

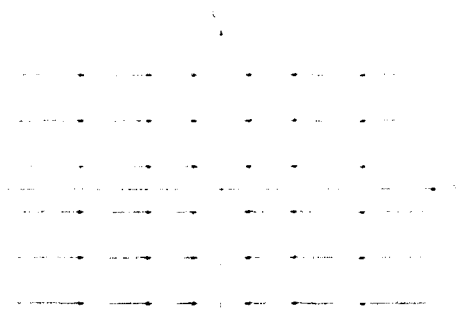


Fig. 1a

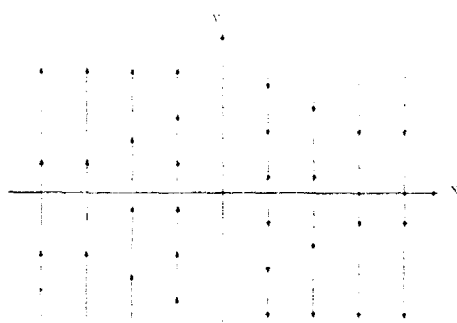


Fig. 1b

Fig. 1. Illustration of surface current variations in the vicinity of an ocean front: (a) converging current ($du/dx < 0$, $dv/dx = 0$) and (b) shearing current ($du/dx = 0$, $dv/dx < 0$).

and

$$\epsilon_r = \left(k_x \frac{du}{dx} + k_y \frac{dv}{dx} \right) \left(\frac{1}{N_0} \frac{\partial N_0}{\partial k_x} f + \frac{\partial f}{\partial k_x} \right) + \gamma N_0 f^2 + \text{higher-order terms.} \quad (5)$$

If the current gradients du/dx and dv/dx are small, the spectral perturbation f is expected to be small as well. Thus ϵ_r contains only second-order and higher-order terms. We can therefore hope to get some insight into the problem by considering the solution of the equation in which ϵ_r is neglected. The validity of this approximation in some cases of interest when the spectral perturbation is not small is discussed in the following section.

Even when ϵ_r is neglected, (3) is difficult to solve in the general case because of the nonconstant coefficient in the first term. However, there are several special cases for which exact solutions of the linearized equation exist. One of these is the case when u is constant, i.e., the strain rate du/dx is zero, so the only current gradients are in the flow parallel to the front, as illustrated in Figure 1b. In this case, (3) does have constant coefficients and can be readily solved by using the integrating factor $\exp \{-\beta_r x / (c_{gx} + u)\}$, to yield

$$f(x) = \frac{1}{c_{gx}} \int_{x_0}^x \mu(x, k_x, k_y) e^{-\beta_r (x-x_0)/(c_{gx}+u)} dx + f(x_0) e^{-\beta_r (x-x_0)/(c_{gx}+u)} \quad du/dx = 0 \quad (6)$$

where $c_{gx} = c_{gx} - u$. When, in addition, the rate of shear (or vorticity) dv/dx is constant, this reduces further to

$$f(x) = \frac{\mu}{\beta_r} + \left[f(x_0) - \frac{\mu}{\beta_r} \right] e^{-\beta_r (x-x_0)/(c_{gx}+u)} \quad (7)$$

$$du/dx = 0, \quad dv/dx = \text{constant.}$$

For the case in which the strain rate du/dx is constant but not zero, (3) no longer has constant coefficients, but a solution can still be found by using the integrating factor

$$\lambda(x) = \exp \{ \beta' \ln (c_{gx} + u) \} = (c_{gx} + u)^{\beta'} \quad (8)$$

where $\beta' = \beta_r (du/dx)^{-1}$. Assuming that the shear rate dv/dx is also constant, the solution can be written in the form

$$f(x) = \frac{\mu}{\beta_r} + \left[f(x_0) - \frac{\mu}{\beta_r} \right] \frac{\lambda(x_0)}{\lambda(x)} \quad (9)$$

$$du/dx = \text{constant}, \quad dv/dx = \text{constant.}$$

It is also instructive to consider two limiting cases relative to the relaxation rate β_r . In the "lossless" limit, i.e., for $\beta_r = 0$, the above solution for $du/dx \neq 0$ approaches

$$f(x) = f(x_0) + \mu \left(\frac{du}{dx} \right)^{-1} \ln \left[\frac{c_{gx} + u(x)}{c_{gx} + u(x_0)} \right] \quad (10)$$

$$\beta_r = 0, \quad du/dx \neq 0$$

which reduces, for the case $du/dx = 0$, to

$$f(x) = f(x_0) + \mu \frac{x - x_0}{c_{gx} + u} \quad \beta_r = 0, \quad du/dx = 0. \quad (11)$$

In the opposite limit, as $\beta_r \rightarrow \infty$, both of the above solutions approach

$$f(x) = \mu / \beta_r, \quad \beta_r \gg (c_{gx} + u) / L \quad (12)$$

where L is a characteristic length scale for the current pattern. This solution is obvious by inspection of (3), and furthermore, it can be seen to hold also at the locations where $c_{gx} + u = 0$ for any nonzero β_r . This is the well-known "blocking" or "resonance" condition.

Although derived for a constant or uniform current gradient, the above solutions can be applied to an arbitrary current field by breaking it up into a set of piecewise linear segments. For the purpose of exploring the general behavior of the wave-current interactions near an ocean front, however, the current field can be approximated by the simple ramp functions

$$\begin{aligned} u(x) &= u_1 & x < -w \\ u(x) &= -u_1 x / w & -w < x < w \\ u(x) &= -u_1 & x > w \end{aligned} \quad (13)$$

and

$$\begin{aligned} v(x) &= v_1 & x < -w \\ v(x) &= -v_1 x / w & -w < x < w \\ v(x) &= -v_1 & x > w \end{aligned} \quad (14)$$

which imply a strain rate $du/dx = -u_c/w$ and a shear rate $dv/dx = -v_c/w$ in the central region.

The solution is evaluated at any given location by first determining the appropriate value of x_0 on the basis of the sign of $c_{gx} + u$. For $c_{gx} + u > 0$ the boundary condition is applied at the left boundary of the region under consideration, i.e., at $x_0 = -w$ for points inside the region $-w < x < w$ and at $x_0 = w$ for points in the region $x > w$. The appropriate boundary value for this case is $f(x) = 0$ for $x \leq -w$. For $c_{gx} + u < 0$ the boundary condition is applied at the right boundary, and the boundary value is $f(x) = 0$ for $x \geq w$.

3. SPECTRAL PERTURBATIONS INDUCED BY OCEAN FRONTS

The spectral perturbations caused by the shearing and converging currents in an ocean front depend on the wind speed and direction (through the relaxation rate β_r and the equilibrium spectrum N_0) as well as the current field. Using the Hughes [1978] formulation for the net source function, the relaxation rate can be considered to be approximately equivalent to the initial growth rate β . On the basis of wave tank measurements as well as theoretical considerations, Plant and Wright [1977] proposed a growth rate of the form

$$\beta = 0.04(u_*/c)^2 \omega \quad (15)$$

where u_* is the friction velocity (which is roughly 1/30 of the wind speed U measured at a standard height of 19.5 m above the surface), c is the phase velocity, and ω is the frequency of the waves. The dependence of β on the wave propagation direction relative to the wind direction could not be observed in the linear wave tank used for these measurements. However, Plant [1986] has suggested an angular dependence of the form

$$\begin{aligned} F(\phi) &= \cos(\phi - \phi_w) & |\phi - \phi_w| < \pi/2 \\ F(\phi) &= 0 & |\phi - \phi_w| > \pi/2 \end{aligned} \quad (16)$$

where ϕ_w is the wind direction.

The equilibrium spectrum enters this solution through its logarithmic gradient

$$\frac{k}{N_0} \frac{\partial N_0}{\partial k} = \frac{k}{N_0} \frac{\partial N_0}{\partial k} \cos \phi - \frac{1}{N_0} \frac{\partial N_0}{\partial \phi} \sin \phi \quad (17)$$

where N_0 is the action spectral density, which is related to the energy spectrum $E_0(k, \phi)$ and the wave height spectrum $S_0(k, \phi)$ through the equation [Phillips, 1980]

$$N_0(k, \phi) = \frac{1}{\omega} E_0(k, \phi) = \rho \frac{\omega}{k} S_0(k, \phi) \quad (18)$$

where k is the magnitude of the wave number and ω is the intrinsic wave frequency, which is given by

$$\omega^2 = gk + (T/\rho)k^3 \quad (19)$$

where g is the gravitational acceleration, T is the surface tension, and ρ is the density of water ($T/\rho = 74 \text{ cm}^3/\text{s}^2$ for a clean water surface).

For wave numbers much larger than the peak wave number $k_0 \approx g/U^2$, the equilibrium wave height spectrum can be modeled as a power law, i.e.,

$$S_0(k, \phi) = F_0(\phi) k^{-p} \quad (20)$$

where $p \approx 4$ in the gravity region and $p \approx 8$ in the capillary region. The angular dependence of the spectrum may be represented by the function

$$F_0(\phi) = c_n \cos^{2n} \left(\frac{\phi - \phi_w}{2} \right) \quad (21)$$

where $n \approx 2-5$ in the intermediate region of the spectrum, and $n \approx 10$ near the peak of the spectrum [Pierson and Stacy, 1973]. Using these forms, the factor μ in (4) can be written as

$$\begin{aligned} \mu = \left(\frac{du}{dx} \cos \phi + \frac{dv}{dx} \sin \phi \right) & \left[-(p+1 - c_g/c) \cos \phi \right. \\ & \left. + n \tan \left(\frac{\phi - \phi_w}{2} \right) \sin \phi \right] \end{aligned} \quad (22)$$

The factor μ is therefore of the same order of magnitude as the current gradients, which are in the range of 0.01–0.001 s^{-1} for moderately strong ocean fronts. The relaxation rate is typically of the order of 0.1–1.0 s^{-1} for wavelengths from 1 to 10 cm and moderate wind speeds. Thus the fractional spectral perturbations predicted by this model are typically only a few percent in this wavelength range. On the other hand, much larger fractional perturbations are predicted for longer wavelengths, where the relaxation rate is much smaller.

At this point, before presenting some examples to illustrate the behavior described in the previous paragraph, it is worth mentioning two problems that occur when the relaxation rate β_r is equated with the growth rate β as discussed at the beginning of this section. The first problem is associated with the angular dependence of β . Using the angular dependence shown in (16), the growth rate falls to zero for waves traveling at angles larger than 90° with respect to the wind direction. If the same angular dependence is assumed for the relaxation rate β_r , unrealistically large spectral perturbations are predicted at these angles, as shown by (10)–(12). The other problem occurs when the growth rate is corrected for viscous dissipation effects. The proper correction to the growth rate is to subtract $4\nu k^2$ from β , where ν is the kinematic viscosity [Plant and Wright, 1977]. However, if this is done, the net growth rate becomes negative at high wave numbers or at large angles to the wind. Obviously, the relaxation rate cannot be simply equated to the net growth rate in these spectral regions, since the relaxation rate must be positive.

The solution to both of these problems is to use a more consistent model for the net source function and to calculate the equilibrium spectrum by solving the equation $f_s(N_0) = 0$. Steps in this direction have been taken, for example, by Donelan and Pierson [1987] and Plant [1986]. The simplest such model would consist of a wind-forcing term proportional to N and a dissipation term proportional to N^p where $p > 1$. If viscous dissipation is included in such a model, the relaxation rate $\beta_r = f_s(N_0)$ still vanishes as the net growth rate ($\beta - 4\nu k^2$) approaches zero, leading to large fractional perturbations. However, the equilibrium spectrum also approaches zero at these points, so the perturbed spectrum $N = N_0(1 + f)$ remains finite, at least if $p < 2$.

A somewhat more satisfactory result is obtained if another source term which is independent of N is added to $f_N(N)$. In that case the equilibrium spectrum and the relaxation rate are both positive for all wave numbers. The equilibrium spectrum is given by the solution of the equation

$$f_S(N_0) = (\beta - 4\nu k^2)N_0 - \gamma N_0^p + \Pi = 0 \quad (23)$$

where Π is the constant term (which physically corresponds to the Phillips resonant growth mechanism), and the relaxation rate is then given by

$$\beta_r = -f_S(N_0) = (p-1)(\beta - 4\nu k^2) + p\frac{\Pi}{N_0} \quad (24)$$

For moderate wind speeds, wavelengths larger than a few centimeters, and wave propagation directions within 90° of the wind direction, the constant term in (23) is negligible in comparison with the first two terms, and it follows that

$$\beta_r \approx (p-1)(\beta - 4\nu k^2) \approx (p-1)\beta \quad (25)$$

in this region. On the other hand, when $4\nu k^2 > \beta$, the equilibrium state is determined by the balance between the first and last terms in (23), so that $N_0 \approx \Pi/(4\nu k^2 - \beta)$ and

$$\beta_r \approx 4\nu k^2 - \beta \approx 4\nu k^2 \quad (26)$$

The relaxation rate thus appears to be the larger of $(p-1)\beta$ and $4\nu k^2$, at least in the extreme cases (what happens in the intermediate region, where $(p-1)\beta \approx 4\nu k^2$, is not yet clear). For order-of-magnitude estimates we have therefore approximated the relaxation rate as

$$\beta_r \approx (p-1)\beta + 4\nu k^2 \quad (27)$$

with $p = 2$. To avoid the discontinuity in the derivative of $\beta(\phi)$ at $\phi - \phi_w = \pi/2$ implied by (16) and to allow for some variability in the wind direction, we have also chosen the angular dependence

$$F(\phi) = \cos^2\left(\frac{\phi - \phi_w}{2}\right) \quad (28)$$

for the growth rate. Finally, in lieu of a complete, self-consistent formulation of the net source function as discussed above, we have used the equilibrium spectrum proposed by Bjerkaas and Riedel [1979] with a $\cos^4(\phi/2)$ angular dependence.

To illustrate the general behavior of the solution, some results were generated using the current pattern specified by (13) and (14) with $u_c = v_c = 5$ cm/s and $w = 10$ m, for a wind speed of 5 m/s along the y axis, parallel to the front. A contour plot showing the wave number dependence of the spectral perturbation at the center of the current pattern ($x = 0$) is presented in Figure 2. The radial distance on this plot represents the logarithm of the wave number, and the angle corresponds to the wave propagation direction. Thus points falling along a vertical line through the center of the plot represent waves traveling parallel to the front. The dashed curves represent the locus of points with a given wavelength as indicated on the plot. The solid curves represent linearly spaced contours of the dimensionless quantity

$$k^4[S(k, \phi) - S_0(k, \phi)] = k^4 S_0(k, \phi) f(k, \phi) \quad (29)$$

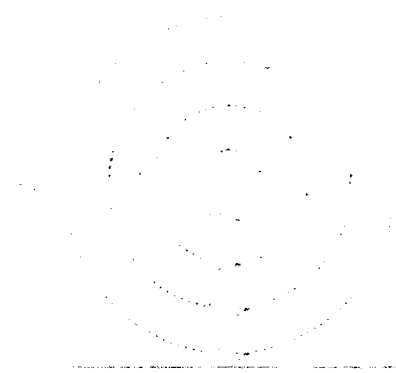


Fig. 2. Contour plot of the spectral perturbation function for $du/dx = dv/dx = -0.005 \text{ s}^{-1}$ with a wind speed of 5 m/s parallel to the front.

where S_0 is the equilibrium height spectrum and f is the fractional spectral perturbation. The peak value of this function occurs at a wavelength of approximately 1 m and a wave propagation direction of about 60° relative to the x axis. A minimum occurs at nearly the same wavelength for a wave propagation direction of about 108° , and another maximum occurs for slightly shorter waves propagating almost directly into the front, from right to left. Plots of the fractional spectral perturbations at these wavelengths and directions versus position are shown in Figure 3.

The wave number dependence of the spectral perturbation function shown in Figure 2 is related to the wave number dependence of N_0 and β_r and is also a result of the combined effects of the shearing and converging currents in the front. If there were only converging currents, as shown in Figure 1a, the spectral perturbation would be an even function of k_x for a wind direction parallel to the front. On the other hand, if there were only shearing currents, as shown in Figure 1b, the spectral perturbation would be an odd function of k_x , with positive values for $k_x > 0$ and negative values for $k_x < 0$ for the geometry assumed in this example. Thus the large peak at $\phi = 60^\circ$ in Figure 1 is due to a reinforcement of the effects of shear and convergence, while the smaller peak at $\phi = 180^\circ$ and the minimum at $\phi = 108^\circ$ are due to a partial cancellation of these effects.

Figure 3 shows that the fractional spectral perturbation is larger than 1 at some locations, which raises a question as to the validity of the linearized solution used for these calculations. In order to address this question, the "source" term $\mu(x, k_x, k_y)$ and the "error" term $\epsilon_r(x, k_x, k_y)$ in (3) were calculated and are plotted in Figures 4-6 for the same wavelengths and directions as used in Figure 3. Figure 4 shows that ϵ_r becomes an appreciable fraction of μ as the spectral perturbation approaches 1. However, since the spectral perturbation depends on the integral of these terms, the accumulated effect of the error term is only about 25% at the right-hand boundary of the current pattern. Note that ϵ_r and μ have the same sign within the current pattern, so the linearized equation underestimates the spectral perturbation in this region. Outside the region where the current is varying (i.e., for $x > 10$ m), ϵ_r is negative, which implies that the full solution decays somewhat more rapidly than the

linearized solution in this region. These conclusions have been confirmed by spot comparisons with "exact" calculations using the numerical model described by *Lyzena and Bennett* [1988].

A similar analysis of Figures 5 and 6 shows that the magnitude of the negative perturbations in the vicinity of $\phi = 108^\circ$ are slightly overestimated, and the positive perturbations around $\phi = 180^\circ$ are slightly underestimated by the linearized model. For wave numbers well away from these peaks, ϵ_r is typically much smaller than μ , indicating that the linearized model performs quite well, as expected. The spectral perturbations predicted by this model at a wavelength of 5 cm are well under 10% for all angles of propagation.

4. RADAR IMAGING OF OCEAN FRONTS

The scattering of microwave radiation from the ocean surface is commonly assumed to be described by the Bragg scattering model, according to which the backscattering radar cross section per unit area is given by

$$\sigma_0(\theta, \phi) = 8\pi k_0^4 G(\theta) \Gamma(\theta) \quad (30)$$

where θ is the incidence angle and ϕ is the azimuthal look angle, k_0 is the electromagnetic wave number, $G(\theta)$ is a polarization-dependent geometric factor given by

$$G_H(\theta) = \frac{\cos^4 \theta}{[1 + (1/\sqrt{\epsilon}) \cos \theta]^4} \quad (31)$$

for horizontal polarization and

$$G_V(\theta) = \frac{\cos^4 \theta (1 + \sin^2 \theta)^2}{[\cos \theta + (1/\sqrt{\epsilon})]^4} \quad (32)$$

for vertical polarization, where $\epsilon \gg 1$ is the relative dielectric constant of seawater, and

$$\Gamma(\theta) = S(k_B, \phi) + S(k_B, \phi + \pi) \quad (33)$$

where $S(k, \phi)$ is the surface elevation spectrum and $k_B = 2k_0 \sin \theta$ is the Bragg resonant surface wave number.

Combining this model directly with the results described in the previous section, we would expect ocean fronts to be very rarely detectable by radars operating at wavelengths in the 1- to 10-cm range, since the predicted changes in the surface spectrum at the Bragg wavelength are typically only a few percent. However, several instances of such detection have been reported [*Johannessen et al.*, 1991; *F. Askari et al.*, An estuarine front viewed by an imaging radar, submitted to *Journal of Geophysical Research*, 1991] for imaging radars operating at C band (5 cm) and X band (3 cm). The fractional changes in backscatter for these cases are of the order of 1 or larger. If the wave-current interaction model described above is assumed to yield an adequate representation of the changes in surface roughness associated with these fronts, then the dominant effects on the radar backscatter must be due to surface waves longer than the Bragg wavelength.

The effects of longer surface waves can be included in the Bragg model by means of a procedure described heuristically by *Wright* [1968] and rederived by *Brown* [1978], *Valenzuela* [1978], *Thompson* [1988], and others, using various methods. Intuitively, these effects can be thought of as being due to changes in the local angle of incidence caused by the tilting

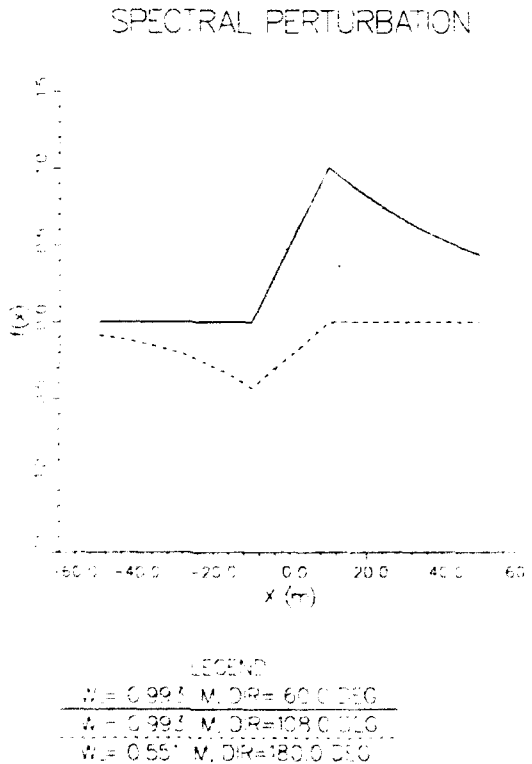


Fig. 3. Fractional spectral perturbation versus position, at the three wavelengths and directions indicated in legend.

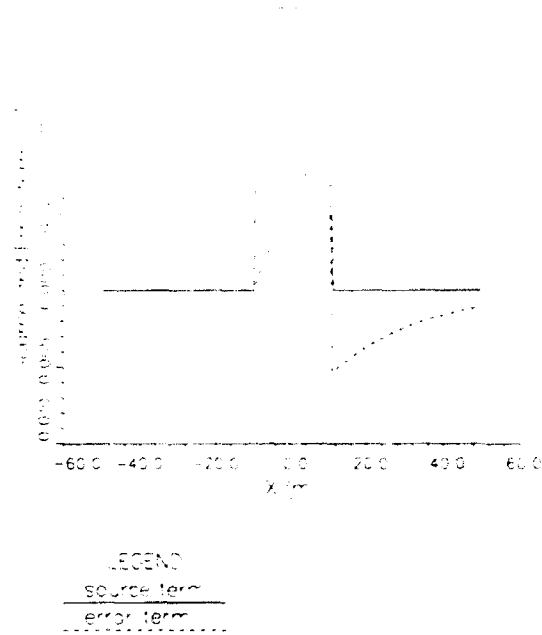


Fig. 4. Magnitude of the source term $\mu(x, k_x, k_y)$ and error term $\epsilon_r(x, k_x, k_y)$ for $\lambda = 0.99$ m and $\phi = 60^\circ$.

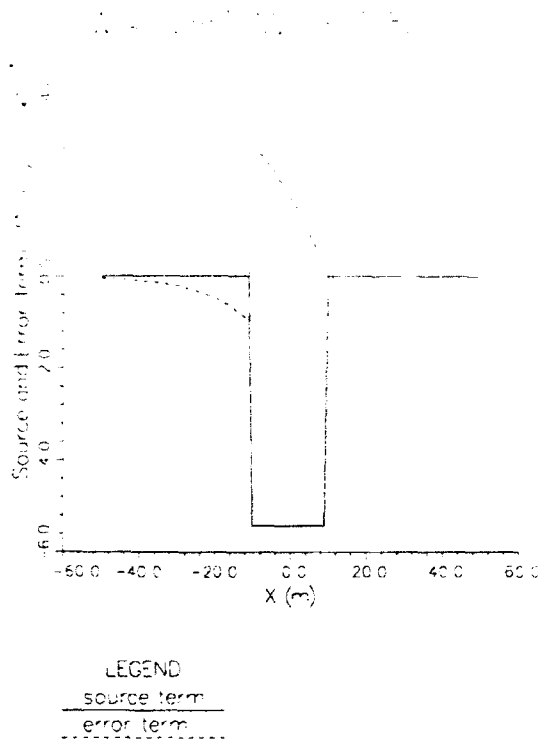


Fig. 5. Magnitude of the source term $\mu(x, k_x, k_y)$ and error term $\epsilon_r(x, k_x, k_y)$ for $\lambda = 0.99$ m and $\phi = 108^\circ$.

of the surface by the longer waves. Since the radar cross section is a nonlinear function of the incidence angle, averaging over all the slopes occurring on the surface results in a net change in the mean backscattered power, even though the mean slope is zero.

Using this approach, an expression for the radar cross section can be derived in terms of the long-wave slope variances $\langle \eta_1^2 \rangle$ and $\langle \eta_2^2 \rangle$ in the plane of incidence and in the perpendicular direction, respectively [Plant, 1986]. A change in η_1 is equivalent to a change in the local incidence angle θ , while a change in η_2 causes a change in the polarization of the incident radiation relative to the local normal. Assuming the mean slope is zero, the mean radar cross section including these effects to second order in the surface slope is

$$\bar{\sigma}_0(\theta, \phi) = \sigma_0(\theta, \phi) \left[1 + \frac{\mu_1}{2} \langle \eta_1^2 \rangle + \frac{\mu_2}{2} \langle \eta_2^2 \rangle \right] \quad (34)$$

where

$$\mu_1 = \frac{1}{\sigma_0} \left(\frac{\partial^2 \sigma_0}{\partial \theta^2} \right) = \frac{G''(\theta)}{G(\theta)} + 2 \frac{G'(\theta)\Gamma'(\theta)}{G(\theta)\Gamma(\theta)} + \frac{\Gamma''(\theta)}{\Gamma(\theta)} \quad (35)$$

and

$$\mu_2 = \frac{1}{\sigma_0} \left(\frac{\partial^2 \sigma_0}{\partial \alpha^2} \right) = \frac{2(2\sqrt{R} - 1)}{\sin^2 \theta} \quad (36)$$

where $\alpha = \tan^{-1} \eta_2$ is the tilt angle perpendicular to the plane of incidence, $R = G_V/G_H$ for horizontal polarization, and $R = G_H/G_V$ for vertical polarization [Plant, 1988].

The sensitivity factor μ_1 can be expressed in terms of the tilt modulation transfer function

$$m(\theta) = \frac{1}{\sigma_0} \left(\frac{\partial \sigma_0}{\partial \theta} \right) = \frac{G'(\theta)}{G(\theta)} + \frac{\Gamma'(\theta)}{\Gamma(\theta)} \quad (37)$$

as

$$\mu_1 = \frac{1}{\sigma_0} \frac{\partial}{\partial \theta} [m\sigma_0] = m'(\theta) + m^2(\theta). \quad (38)$$

Using the above expressions for $G_H(\theta)$ and $G_V(\theta)$, the polarization-dependent part of $m(\theta)$ can be written as

$$m_H(\theta) = \frac{G'_H(\theta)}{G_H(\theta)} = \frac{4 \sin \theta}{\sqrt{\epsilon} + \cos \theta} - 4 \tan \theta \quad (39)$$

for horizontal polarization and

$$m_V(\theta) = \frac{G'_V(\theta)}{G_V(\theta)} = \frac{4 \sin \theta}{(1/\sqrt{\epsilon}) + \cos \theta} - \frac{8 \sin^2 \theta \tan \theta}{1 + \sin^2 \theta} \quad (40)$$

for vertical polarization. Finally, if the symmetrized spectrum can be expressed as a power law in k , i.e.,

$$S(k, \phi) + S(k, \phi + \pi) = A(\phi)k^{-p} \quad (41)$$

then the polarization-independent part of $m(\theta)$ can be written as

$$m_S(\theta) = \Gamma'(\theta)/\Gamma(\theta) = -p \cot \theta. \quad (42)$$

Perturbations in the wave spectrum can thus be seen to affect the radar backscatter in three ways, according to this model: (1) through changes in the spectral density at the Bragg wave number, (2) through changes in the large-scale slope variances $\langle \eta_1^2 \rangle$ and $\langle \eta_2^2 \rangle$, and (3) through changes in the

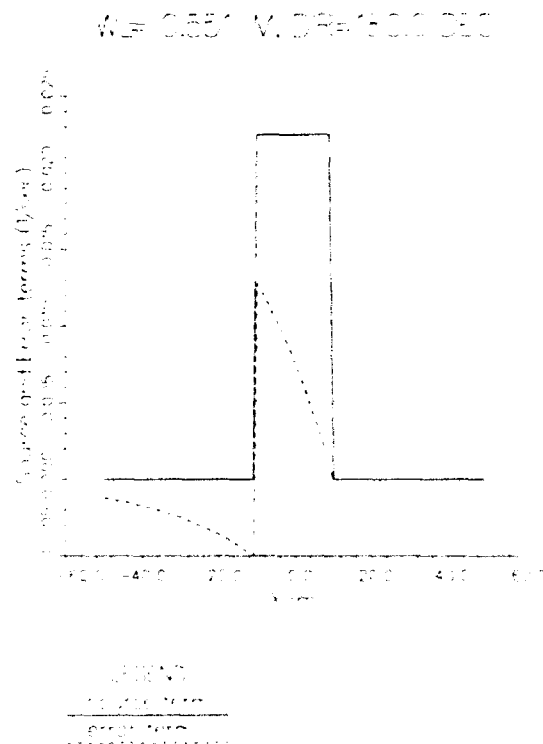


Fig. 6. Magnitude of the source term $\mu(x, k_x, k_y)$ and error term $\epsilon_r(x, k_x, k_y)$ for $\lambda = 0.55$ m and $\phi = 180^\circ$.

gradient of the spectrum near the Bragg wave number (i.e., the value of p).

On the basis of the predictions of the wave-current interaction model discussed in section 3, the second of these would appear to be the dominant mechanism for imaging ocean fronts at the higher microwave frequencies (C and X band), since only small changes in the wave spectrum are predicted at the Bragg wave numbers for these radar frequencies. The values of $\mu_1/2$ and $\mu_2/2$ are typically of the order of 10–100, depending on the incidence angle and polarization [Plant, 1986, 1988]. Thus changes in the slope variance of the order of 0.01 can cause substantial changes in the radar cross section and could explain at least qualitatively the appearance of frontal-related features in such images.

For the example case discussed in section 3, the maximum change in the X band radar cross section at a 20° incidence angle is about 1 dB, as shown in Figure 7. Such a feature would be visible within the speckle or Rayleigh noise background of a radar image. However, the magnitude of this change decreases rapidly with increasing incidence angle, particularly for vertical polarization, as shown in Figures 8 and 9. The backscatter variations shown in these plots would be barely visible or not detectable, depending on the radar resolution. On the other hand, the backscatter modulations observed in the existing data sets appear to be roughly independent of incidence angle. Consequently, it is not clear that the type of model described in this paper is capable of adequately explaining the observed backscatter modulations at intermediate incidence angles, even though it appears to do so at small incidence angles.

5. CONCLUSIONS

Changes in surface roughness can be caused by the interaction of surface waves with both the converging and

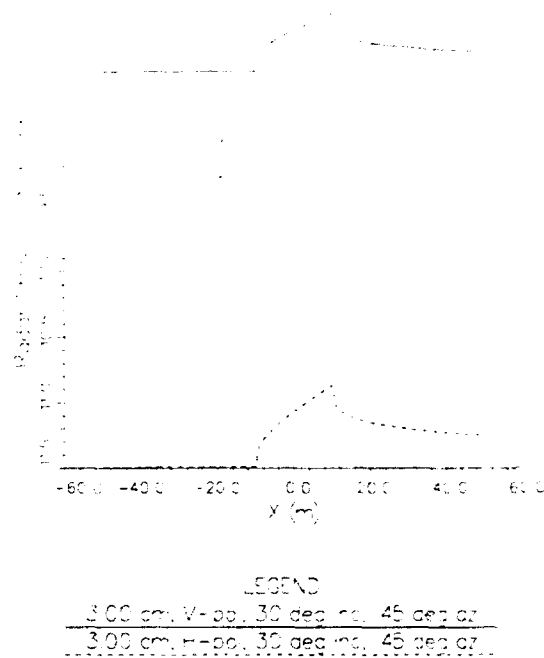


Fig. 8. Backscatter variation predicted by two-scale model at X band, 30° incidence for test case discussed in text.

the shearing currents associated with ocean fronts. The largest spectral perturbations typically occur at wavelengths of the order of 1 m. The perturbations decrease at longer wavelengths when the group velocity becomes much larger

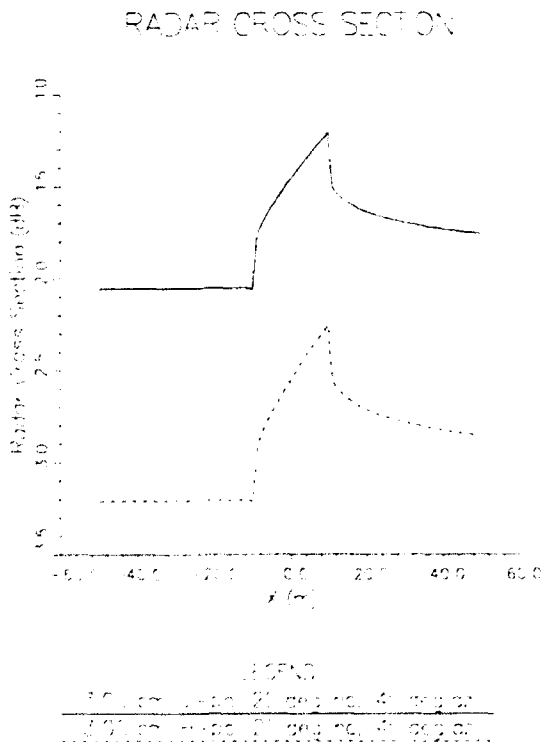


Fig. 7. Backscatter variation predicted by two-scale model at X band, 20° incidence for test case discussed in text.

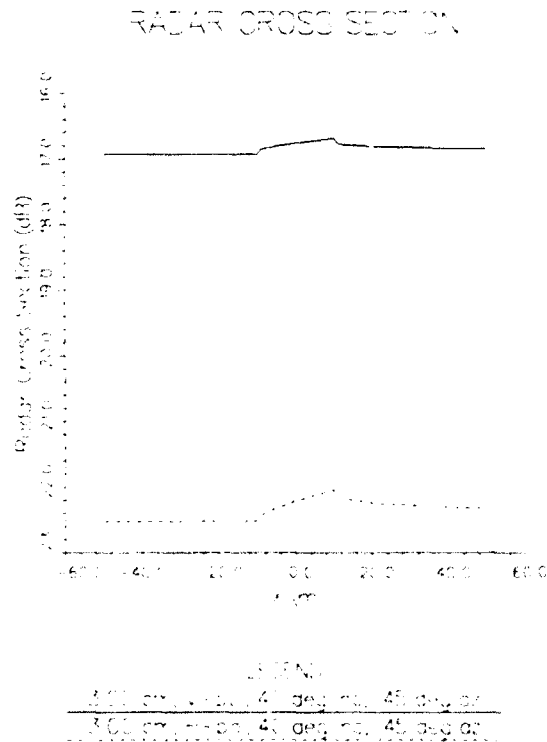


Fig. 9. Backscatter variation predicted by two-scale model at X band, 40° incidence for test case discussed in text.

than the current speed and at shorter wavelengths where relaxation effects play a predominant role. The shape of the spectral perturbation function depends on the wind direction and is also influenced by the nature of the currents, with the effects of shearing and converging currents tending to reinforce each other in certain spectral regions and to cancel each other in other regions.

Because of the small spectral perturbations predicted at centimeter wavelengths, simple Bragg scattering does not appear to be sufficient to explain the appearance of fronts in radar images collected at C band and higher frequencies. A qualitative explanation is provided by the two-scale scattering model, which introduces a coupling between the long-wave spectral perturbations and the radar backscatter. However, this coupling is relatively weak at intermediate incidence angles, and it is not yet clear that the observed backscatter variations at these angles are adequately explained by this model. Consequently, additional hydrodynamic and/or electromagnetic effects which are not presently accounted for may be important in some cases. For example, nonlinear wave-wave interactions or wave breaking may result in the cascade of energy from the longer waves down to centimeter wavelengths, necessitating additional nonlocal source terms in the wave action equation. Furthermore, the surface statistics associated with highly nonlinear or breaking waves may violate the assumptions of the two-scale model and require a reexamination of the scattering problem.

Acknowledgments. This work was supported by the Office of Naval Research, contract N00014-90-C-0071.

REFERENCES

- Bjerkaas, A. W., and F. W. Riedel. Proposed model for the elevation spectrum of a wind-roughened surface. *Rep. TG-1328*, 31 pp., Appl. Phys. Lab., Johns Hopkins Univ., Laurel, Md., 1979.
- Brown, G. S., Backscattering from a Gaussian-distributed perfectly conducting rough surface. *IEEE Trans. Antennas Propag.*, AP-26, 472-482, 1978.
- Donelan, M. A., and W. J. Pierson, Radar scattering and equilibrium ranges in wind-generated waves with application to scatterometry. *J. Geophys. Res.*, 92, 4971-5029, 1987.
- Fu, L. L., and B. Holt. Some examples of detection of oceanic mesoscale eddies by the Seasat synthetic aperture radar. *J. Geophys. Res.*, 88, 1844-1852, 1983.
- Garvine, R. W., and J. D. Monk. Frontal structure of a river plume. *J. Geophys. Res.*, 79, 2251-2259, 1974.
- Hayes, R. M., SAR detection of the Gulf Stream, in *Spaceborne Synthetic Aperture Radar for Oceanography*, edited by R. C. Beal, P. DeLeonibus, and I. Katz, pp. 146-160. Johns Hopkins Press, Baltimore, Md., 1981.
- Hughes, B. A., The effect of internal waves on surface wind waves. 2. Theoretical analysis. *J. Geophys. Res.*, 83, 455-465, 1978.
- Johannessen, J. A., R. A. Shuchman, O. M. Johannessen, K. L. Davidson, and D. R. Lyzenga. Synthetic aperture radar imaging of upper ocean circulation features and wind fronts. *J. Geophys. Res.*, in press, 1991.
- Larson, T. R., L. I. Moskowitz, and J. W. Wright. A note on SAR imagery of the ocean. *IEEE Trans. Antennas Propag.*, AP-24, 393-394, 1976.
- Lyzenga, D. R., and J. R. Bennett. Full-spectrum modeling of synthetic aperture radar internal wave signatures. *J. Geophys. Res.*, 93, 12,345-12,354, 1988.
- Mattie, M. G., D. E. Lichy, and R. C. Beal. Seasat detection of waves, currents and inlet discharge. *Int. J. Remote Sens.*, 1, 377-398, 1980.
- Phillips, O. M., *The Dynamics of the Upper Ocean*, 1st paperback ed., 336 pp., Cambridge University Press, New York, 1980.
- Phillips, O. M., On the response of short ocean wave components at a fixed wavenumber to ocean current variations. *J. Phys. Oceanogr.*, 14, 1425-1433, 1984.
- Pierson, W. J., and R. A. Stacy. The elevation, slope, and curvature spectra of a wind roughened sea surface. *NASA Rep.*, CR-2247, 129 pp., 1973.
- Plant, W. J., A two-scale model of short wind-generated waves and scatterometry. *J. Geophys. Res.*, 91, 10,735-10,749, 1986.
- Plant, W. J., Correction to "A two-scale model of short wind-generated waves and scatterometry." *J. Geophys. Res.*, 93, 1347, 1988.
- Plant, W. J., and J. W. Wright. Growth and equilibrium of short gravity waves in a wind-wave tank. *J. Fluid Mech.*, 82, 767-793, 1977.
- Thompson, D. R., Calculation of radar backscatter modulations from internal waves. *J. Geophys. Res.*, 93, 12,371-12,380, 1988.
- Valenzuela, G. R., Theories for the interaction of electromagnetic and oceanic waves—A review. *Boundary Layer Meteorol.*, 13, 61-85, 1978.
- Vesecky, J. F., and R. H. Stewart. The observation of ocean surface phenomena using imagery from the Seasat synthetic aperture radar: An assessment. *J. Geophys. Res.*, 87, 3397-3430, 1982.
- Wright, J. W., A new model for sea clutter. *IEEE Trans. Antennas Propag.*, AP-16, 217-223, 1968.
- D. R. Lyzenga, Advanced Concepts Division, Environmental Research Institute of Michigan, P.O. Box 8618, Ann Arbor, MI 48107.

(Received November 20, 1990;
revised March 26, 1991;
accepted March 26, 1991.)